

Journal Pre-proof

Intermetallic compound PtMn_y -derived $\text{Pt}_{\text{null}}\text{MnO}_x$ supported on mesoporous CeO_2 : Highly efficient catalysts for the combustion of toluene

Xiaohang Fu, Yuxi Liu, Jiguang Deng, Lin Jing, Xing Zhang, Kunfeng Zhang, Zhuo Han, Xiyun Jiang, Hongxing Dai



PII: S0926-860X(20)30102-2
DOI: <https://doi.org/10.1016/j.apcata.2020.117509>
Reference: APCATA 117509
To appear in: *Applied Catalysis A, General*
Received Date: 2 February 2020
Revised Date: 1 March 2020
Accepted Date: 2 March 2020

Please cite this article as: Fu X, Liu Y, Deng J, Jing L, Zhang X, Zhang K, Han Z, Jiang X, Dai H, Intermetallic compound PtMn_y -derived $\text{Pt}_{\text{null}}\text{MnO}_x$ supported on mesoporous CeO_2 : Highly efficient catalysts for the combustion of toluene, *Applied Catalysis A, General* (2020), doi: <https://doi.org/10.1016/j.apcata.2020.117509>

This is a PDF file of an article that has undergone enhancements after acceptance, such as the addition of a cover page and metadata, and formatting for readability, but it is not yet the definitive version of record. This version will undergo additional copyediting, typesetting and review before it is published in its final form, but we are providing this version to give early visibility of the article. Please note that, during the production process, errors may be discovered which could affect the content, and all legal disclaimers that apply to the journal pertain.

© 2020 Published by Elsevier.

Intermetallic compound PtMn_y-derived Pt–MnO_x supported on mesoporous CeO₂: Highly efficient catalysts for the combustion of toluene

Xiaohang Fu, Yuxi Liu*, Jiguang Deng, Lin Jing, Xing Zhang, Kunfeng Zhang, Zhuo Han, Xiyun Jiang, Hongxing Dai*

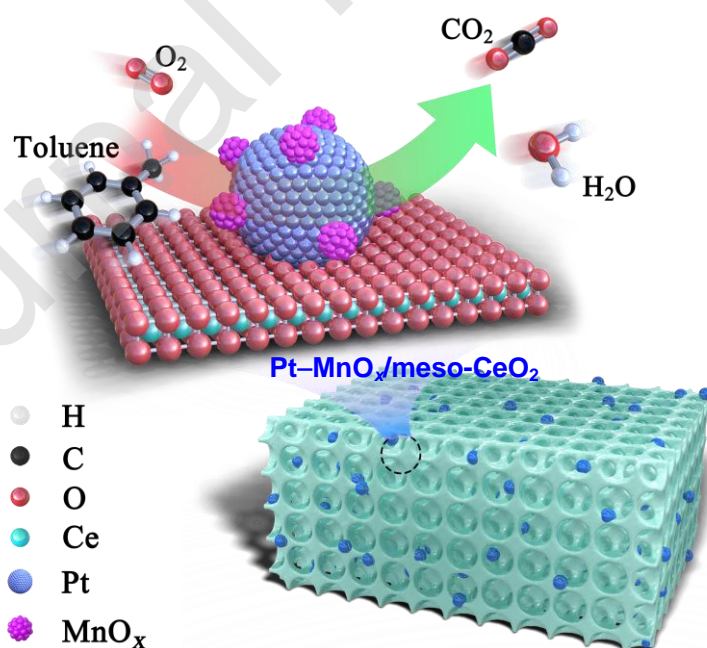
Beijing Key Laboratory for Green Catalysis and Separation, Key Laboratory of Beijing on Regional Air Pollution Control, Key Laboratory of Advanced Functional Materials, Education Ministry of China, Laboratory of Catalysis Chemistry and Nanoscience, Department of Chemistry and Chemical Engineering, College of Environmental and Energy Engineering, Beijing University of Technology, Beijing 100124, China

* Corresponding authors.

E-mail addresses: yxliu@bjut.edu.cn (Dr. Y. Liu); hxdai@bjut.edu.cn (Prof. H. Dai)

Tel. No.: +8610-6739-6118; Fax: +8610-6739-1983.

Graphical abstract



Loading the PtMn_y intermetallic nanocrystals derived from the PVP-assisted EG

reduction route on meso-CeO₂ and after calcination in air generates the Pt–MnO_x/meso-CeO₂ catalysts. The good performance for toluene combustion of 0.37Pt–0.16MnO_x/meso-CeO₂ is related to its high adsorbed oxygen and Mn²⁺ species concentration and good low-temperature reducibility.

Highlights

- PtMn_y intermetallic nanocrystals are fabricated using the PVP-assisted EG reduction method.
- *m*Pt–*n*MnO_x/meso-CeO₂ is prepared via adsorption of PtMn_y NCs on meso-CeO₂.
- 0.37Pt–0.16MnO_x/meso-CeO₂ perform the best for toluene combustion.
- 0.37Pt–0.16MnO_x/meso-CeO₂ exhibits good water-resistant performance.
- O_{ads} and Mn²⁺ concentration, low-temp. reducibility, and toluene adsorption ability govern activity.

Abstract

Intermetallic compounds are a kind of important materials in heterogeneous catalysis. In this work, we first synthesized the PtMn_y intermetallic nanocrystals using the polyvinyl pyrrolidone-assisted ethylene glycol reduction method, and then loaded them on the surface of mesoporous CeO₂ (meso-CeO₂) derived from a KIT-6-templating route, generating the *m*Pt–*n*MnO_x/meso-CeO₂ (*m* = 0–0.39 wt%, *n* = 0–1.21 wt%) catalysts after calcination at 500 °C in air. It is found that the as-obtained catalysts

displayed an ordered mesoporous architecture with surface areas of 95–108 m²/g. The 0.37Pt–0.16MnO_x/meso-CeO₂ sample exhibited the best catalytic performance for toluene combustion ($T_{50\%} = 162$ °C and $T_{90\%} = 171$ °C at space velocity = 40,000 mL/(g h)). Kinetic analysis reveals that the apparent activation energy (57 kJ/mol) obtained over the best-performing 0.37Pt–0.16MnO_x/meso-CeO₂ sample was lower than those (63–75 kJ/mol) obtained over the other samples. Furthermore, the 0.37Pt–0.16MnO_x/meso-CeO₂ sample possessed good thermal stability and water-resistant performance. Benzyl alcohol, benzoic acid, and maleic anhydride were proven to be the main intermediates of toluene combustion, hence, toluene combustion might take place through a sequence of toluene → benzyl alcohol and benzoic acid → maleic anhydride → carbon dioxide and water, which might obey the Eley–Rideal reaction mechanism. It is concluded that loading of Pt and MnO_x enhanced the adsorbed oxygen and Mn²⁺ species concentration and low-temperature reducibility, thus promoting toluene combustion over 0.37Pt–0.16MnO_x/meso-CeO₂.

Keywords: Mesoporous ceria; PtMn intermetallic nanocrystal; Supported Pt–MnO_x catalyst; Volatile organic compound; Toluene combustion.

1. Introduction

Volatile organic compounds (VOCs) are the important precursors of photochemical smog and fine particulate matter (PM_{2.5}), which are harmful to the atmosphere and human being's health [1]. Accordingly, it is highly required to abate VOCs emissions. Among the methods of VOCs removal, catalytic combustion is considered to be the most effective because of its low cost and high efficiency [2,3]. The key to catalytic

combustion of VOCs is generation of the catalysts that are cheap in cost, high in activity, and good in stability.

Although supported Pt catalysts exhibit excellent activity for VOCs combustion at low temperatures [4], they are expensive and easily sintered at high temperatures, which greatly limit their wide applications. To solve these problems, it is a better choice to dope a base metal in Pt nanoparticles (NPs) to reduce the Pt amount and improve the thermal stability. As we know, support plays a remarkable role in improving catalytic activity [5,6]. Owing to excellent oxygen storage and release ability, ceria-based materials have attracted much attention in recent years [7,8]. A higher surface area is favorable for enhancement in activity of a material, and the good strategy to increase surface area is to fabricate the material with an ordered mesoporous architecture.

Intermetallic compounds are the materials comprising two or more elements located left and around the Zintl line in the periodic table [9], and their crystal structures are completely or at least partly ordered and different from those of the constituent elements. Heterogeneous catalysis of intermetallic compounds has been regarded as a quickly developing field [10]. The peculiar combination of the crystal and electronic structures of intermetallic compounds results in their unique adsorption and thus catalytic properties, in which covalent bonding is necessary to stabilize the specific crystal and electronic structure of an intermetallic compound. Such a site preference can provide the catalytic stability under reaction conditions. This makes intermetallic compounds be highly interesting catalytic materials. For example, Armbrüster et al. [11] adopted a co-reduction of the palladium and gallium precursors in organic solvents to prepare the

GaPd or GaPd₂ NPs, and observed that the activity per Pd atom of these materials reached those of the commercially available supported Pd catalysts while preserving the excellent selectivity of the unsupported materials. Osswald et al. [12] reported that nearly no deactivation or loss in selectivity was observed over the Ga₇Pd₃, GaPd or GaPd₂ intermetallic compound as compared with the 5 wt% Pd/Al₂O₃ sample within 20 h of reaction (hydrogenation of acetylene). The high selectivity of the Ga–Pd compounds prevented formation of the carbonaceous deposits and hence these intermetallic compounds showed good stability. To the best of our knowledge, there have been rare works related to the utilization of intermetallic compounds in the application of VOCs combustion. For example, Willis et al. [13] studied promotional effect of the transition metal on methane oxidation over the palladium catalysts, and found that some metals (Fe, Co, and Sn) inhibited sintering of the active Pd metal phase, while the others (Ni and Zn) increased its intrinsic activity as compared with a monometallic Pd catalyst. Therefore, intermetallic compounds are promising materials in heterogeneous catalysis. In recent years, VOCs combustion over the supported bimetallic catalysts has been studied intensively and extensively. For instance, we previously [14] synthesized Au–Pd alloys supported on three-dimensionally ordered macroporous (3DOM) Co₃O₄, and found that the bimetallic catalysts were more active and stable than the single metal counterparts for toluene oxidation. After investigating the one-step seeding growth-derived core-shell Au@Co NPs, Yan et al. [15] pointed out that the Au@Co catalyst was highly active for hydrolytic dehydrogenation of ammonia borane. Ho et al. [16] used the borane–amine reduction method to obtain the

bimetallic MPd (M = Co or Cu) NPs, and claimed that the MPd NPs showed good catalytic performance for formic acid electrooxidation.

In the past several years, our group has prepared 1.67 wt% Mn₃O₄-2 wt% Au/3DOM La_{0.6}Sr_{0.4}CoO₃ [17], 0.25 wt% Pt₁/meso-Fe₂O₃ [18], and 8.5 wt% Co₃O₄/MnO₂ [19] via the polyvinyl alcohol-protecting reduction route, and observed that most of the materials performed well in catalyzing combustion of the typical VOCs (e.g., toluene, benzene, and *o*-xylene). Herein, we first synthesized the PtMn_y intermetallic nanocrystals (NCs) using the polyvinyl pyrrolidone (PVP)-assisted ethylene glycol (EG) reduction method, and then loaded them on the surface of ordered mesoporous CeO₂ (meso-CeO₂), characterized their physicochemical properties of the as-prepared *m*Pt-*n*MnO_x/meso-CeO₂ (*m* = 0-0.39 wt%, *n* = 0-1.21 wt%), and evaluated their catalytic activities for toluene combustion.

2. Experimental

2.1. Catalyst preparation

The ordered mesoporous silica (KIT-6) template was fabricated according to the procedures reported in the literature [20]. Ordered mesoporous CeO₂ (meso-CeO₂) was fabricated by the KIT-6-templating strategy. 2.0 g of the KIT-6 template was added to 40 mL of ethanol containing 4.0 g of Ce(NO₃)₃·6H₂O. The mixture was first dried at room temperature (RT) and calcined at a ramp of 1 °C/min from RT to 600 °C and kept at 600 °C for 6 h. The obtained powders were twice treated in a hot (60 °C) NaOH aqueous solution (concentration = 2.0 mol/L) for the removal of the SiO₂ template, and washed with deionized water and ethanol several times, hence obtaining the meso-CeO₂

support.

The PtMn_y NCs and Pt NPs were synthesized using the PVP-protected EG reduction strategy with an ethanol solution of NaBH₄ as reducing agent. The typical synthesis processes are as follows: The desired amounts of chloroplatinic acid (H₂PtCl₆), manganese acetate (theoretical Mn/Pt molar ratio (*y*) = 0, 2.0, 7.0, and 11.6, which were aimed to control the actual loadings of MnO_x and Pt in the samples), PVP (Pt/PVP mass ratio = 1 : 1.5), and 20 mL of EG were added to 100 mL of two-necked round-bottom flask at 50 °C under stirring. After that, a NaBH₄ ethanol solution (0.75 mol/L, PtMn_y/NaBH₄ molar ratio = 1 : 10) was fast added to generate a black suspension after vigorous stirring for 15 min, hence obtaining the PtMn_y NCs (the actual Mn/Pt molar ratio (*y*) = 1.5, 7.7, and 11.6 (Table1)). The Pt NPs and Mn NPs were fabricated using the above same method in the absence of manganese acetate and chloroplatinic acid, respectively.

The meso-CeO₂-supported PtMn_y NCs (PtMn_y/meso-CeO₂) and Pt NPs (Pt/meso-CeO₂) were prepared via an adsorption route. A desired amount of meso-CeO₂ was added to the above obtained suspension of PtMn_y NCs or Pt NPs (theoretical Pt loading = 0.5 wt%). The suspension was ultrasonically (60 kHz) treated for 15 min and vigorously stirred for 8 h, the wet solid was first filtered and then dried at 50 °C for 12 h, obtaining the PtMn_y/meso-CeO₂ samples. Finally, the PtMn_y/meso-CeO₂ samples were calcined in air at a ramp of 5 °C/min from RT to 500 °C and kept at this temperature for 2 h, thus generating the *m*Pt-*n*MnO_x/meso-CeO₂ (*m* and *n* are the weight percentages of Pt and MnO_x, respectively) samples. Using the inductively coupled

plasma-atomic emission spectroscopic (ICP-AES) technique, we can realize that (i) the actual Pt and MnO_x loadings in the Pt/meso-CeO₂ and MnO_x/meso-CeO₂ samples were 0.39 and 0.16 wt%, respectively; and (ii) the actual Pt (*m*) and MnO_x (*n*) loadings in the *m*Pt-*n*MnO_x samples were 0.37 and 0.16 wt%, 0.36 and 0.78 wt%, and 0.37 and 1.21 wt% (Table 1), respectively. The corresponding samples were denoted as 0.39Pt/meso-CeO₂, 0.16MnO_x/meso-CeO₂, 0.37Pt-0.16MnO_x/meso-CeO₂ (derived from PtMn_{1.5}/meso-CeO₂ after calcination at 500 °C in air), 0.36Pt-0.78MnO_x/meso-CeO₂ (derived from PtMn_{7.7}/meso-CeO₂ after calcination at 500 °C in air), and 0.37Pt-1.21MnO_x/meso-CeO₂ (derived from PtMn_{11.6}/meso-CeO₂ after calcination at 500 °C in air).

All of the chemicals were A.R. in purity, which were purchased from China National Medicines Corporation Ltd.

2.2. Catalyst characterization

Physicochemical properties of meso-CeO₂, 0.16MnO_x/meso-CeO₂, 0.39Pt/meso-CeO₂, and *m*Pt-*n*MnO_x/meso-CeO₂ were measured by means of the ICP-AES, XRD, BET, TEM, XPS, H₂-TPR, O₂-TPD, toluene-TPD, and in situ DRIFTS techniques. The detailed characterization procedures are stated in the Supplementary material.

2.3. Catalytic activity measurement

Catalytic activities of the samples were evaluated in a continuous-flow fixed-bed quartz tubular microreactor (i.d. = 6.0 mm). The sample (50 mg, 40–60 mesh) was diluted with quartz sand (250 mg, 40–60 mesh) for minimizing the effect of possible hot spots. Before the test, the sample was treated in O₂ (20 mL/min) at 250 °C for 1 h.

The reactant gas mixture contained 1000 ppm toluene, 20 vol% O₂, and N₂ (balance), and the total flow was 33.4 mL/min (space velocity (SV) = ca. 40,000 mL/(g h)). 1.0, 3.0, and 5.0 vol% water vapor was introduced to the reaction system through a water saturator at 17, 35, and 45 °C, respectively. 5.0 vol% CO₂ was introduced from a CO₂ cylinder (N₂ as balance gas). Reaction mixtures were online analyzed on a gas chromatograph (GC-2010, Shimadzu) equipped with a flame ionization detector and a thermal conductivity detector, in which a Stabilwax column (30 m in length) and a Carboxen 1000 column (3 m in length) were employed. Only CO₂ was detected in the outlet gas mixture. The balance of carbon in the catalytic system was 99.5 ± 1.5 %. Toluene conversion (X %) was calculated according to the formula: $X = (c_{\text{inlet}} - c_{\text{outlet}})/c_{\text{inlet}} \times 100$ %, in which the c_{inlet} and c_{outlet} are the inlet and outlet toluene concentrations in the feed stream, respectively.

3. Results and discussion

3.1. Crystal phase composition, pore structure, and surface area

Fig. 1A shows XRD patterns of the meso-CeO₂, 0.39Pt/meso-CeO₂, 0.16MnO_x/meso-CeO₂, and $m\text{Pt}-n\text{MnO}_x/\text{meso-CeO}_2$ samples. After referring to XRD pattern (JCPDS PDF# 34-0394) of the standard ceria sample, we can know that CeO₂ in all of the samples possessed a cubic crystal structure, and their crystal planes are shown in Fig. 1A(e). No diffraction signals assigned to the MnO_x and/or Pt phases were observed, a result possibly owing to their low loadings and good dispersion on the surface of meso-CeO₂. In other words, loading of Pt and/or MnO_x did not induce an obvious change in crystal phase of meso-CeO₂. The observation of a weak diffraction peak at $2\theta = \text{ca. } 1^\circ$

in small-angle XRD pattern of each sample (Fig. 1B) means generation of an ordered mesoporous architecture. The calculated grain sizes of meso-CeO₂ in the samples were ca. 10 nm (Table 1).

Shown in Fig. 2A are N₂ sorption isotherms of the meso-CeO₂, 0.39Pt/meso-CeO₂, 0.16MnO_x/meso-CeO₂, and *m*Pt-*n*MnO_x/meso-CeO₂ samples. Each sample displayed a IV-typed isotherm with a hysteresis loop in the relative pressure range of 0.1–1.0, indicating formation of mesopores. As shown in the pore-size distribution (Fig. 2B) of each sample, a peak appeared in the range of 3–6 nm. Textural parameters of the samples are listed in Table 1. There was no significant drop in surface area of the supported Pt, MnO_x or *m*Pt-*n*MnO_x sample. Surface areas, average pore sizes, and pore volumes of the as-prepared samples were 95–108 m²/g, 4.0 nm, and 0.19–0.22 cm³/g, respectively.

Fig. 3 shows TEM images of the samples. The meso-CeO₂ support possessed a good-quality ordered mesopore architecture (Fig. 3a). The lattice spacing (*d* value) of the (200) crystal plane of meso-CeO₂ was measured to be ca. 0.276 nm (Fig. 3b), which was similar to that of the standard CeO₂ sample. After loading the Pt, MnO_x or *m*Pt-*n*MnO_x NPs, the ordered mesoporous structure was well retained (Fig. 3c, e, and g). Due to low loadings, we did not observe the Pt, MnO_x or *m*Pt-*n*MnO_x NPs in the TEM images, but the Pt, MnO_x, and CeO₂ with Pt and MnO_x highly distributed on the surface of meso-CeO₂ were detected in the HADDF-STEM image and elemental mappings of the 0.37Pt-0.16MnO_x/meso-CeO₂ sample (Fig. 4). Fig. 5 shows TEM images and particle-size distribution of PtMn_{1.5} intermetallic NCs. Obviously, the

obtained PtMn_{1.5} NCs were monodispersive and uniform in particle size (ca. 2.2 nm, which was estimated by statistically analyzing particle sizes of 150 NPs). It can be deduced from Figs. 4 and 5 that there was formation of a PtMn_{1.5} intermetallic compound and Pt–MnO_x NPs in the 0.37Pt–0.16MnO_x/meso-CeO₂ sample. That is to say, the adopted preparation methods were effective for generation of the PtMn_y intermetallic compounds and *m*Pt–*n*MnO_x/meso-CeO₂ samples.

3.2. Catalytic performance and effects of moisture and carbon dioxide on activity

Toluene combustion was chosen to evaluate catalytic activities of the samples. Toluene conversions at various temperatures, reaction rate normalized per gram of catalyst, and Arrhenius plots are presented in Fig. 6. When only quartz sand was loaded in the microreactor, no significant toluene conversions (< 2 %) below 300 °C at SV = 40,000 mL/(g h), indicating that no obvious gas-phase reaction took place. In other words, toluene was catalytically oxidized over the samples. When reaction temperature rose, toluene conversion increased monotonously (Fig. 6A). Pt loading resulted in enhancement in activity of the meso-CeO₂ and its supported MnO_x samples. Loading a small amount (0.16 wt%) of MnO_x could improve the catalytic activity, but an excessive amount (0.78 or 1.21 wt%) of MnO_x caused the catalytic activity to decrease. For the sake of better comparison on catalytic performance of the samples, we use the reaction temperatures ($T_{10\%}$, $T_{50\%}$, and $T_{90\%}$), at which 10, 50, and 90 % conversions of toluene were achieved, respectively, as listed in Table 2. Obviously, the 0.37Pt–0.16MnO_x/meso-CeO₂ sample performed the best, with the $T_{10\%}$, $T_{50\%}$, and $T_{90\%}$ being 127, 162, and 171 °C, respectively. Compared to the $T_{50\%}$ and $T_{90\%}$ over the

0.39Pt/meso-CeO₂ sample, those over the 0.37Pt–0.16MnO_x/meso-CeO₂ sample decreased by 19 and 18 °C, respectively. The changing trend in toluene reaction rate normalized per gram of catalyst versus temperature was the same as that in toluene conversion versus temperature (Fig. 6B). Apparent activation energies (E_a) for toluene combustion over the samples (Table 2) were calculated from their Arrhenius plots (Fig. 6C). The E_a obtained over 0.37Pt–0.16MnO_x/meso-CeO₂ was 57 kJ/mol, much lower than those (63–75 kJ/mol) obtained over meso-CeO₂, 0.16MnO_x/meso-CeO₂, 0.39Pt/meso-CeO₂, 0.36Pt–0.78MnO_x/meso-CeO₂, and 0.37Pt–1.21MnO_x/meso-CeO₂. It is well known that the lower the E_a , the better the performance of a catalyst. Hence, the 0.37Pt–0.16MnO_x/meso-CeO₂ sample exhibited the best activity. These results demonstrate that loading Pt and MnO_x with proper amounts favored the augmentation in catalytic performance of toluene combustion.

Catalytic activities for toluene combustion of the 0.37Pt–0.16MnO_x/meso-CeO₂ sample and the catalysts reported in the literature are summarized in Table S1 of the Supplementary material. Apparently, 0.37Pt–0.16MnO_x/meso-CeO₂ ($T_{90\%} = 171$ °C at SV = 40,000 mL/(g h); toluene reaction rate at 160 °C = 0.339 $\mu\text{mol}/(\text{g}_{\text{cat}} \text{s})$) exhibited much better activity than 1 wt% Pt/SBA-15 ($T_{90\%} = 189$ °C at SV = 10,000 h⁻¹; toluene reaction rate at 160 °C = 0.067 $\mu\text{mol}/(\text{g}_{\text{cat}} \text{s})$) [21], 0.27 wt% Pt/3DOM 26.9CeO₂–Al₂O₃ ($T_{90\%} = 198$ °C at SV = 20,000 mL/(g h); toluene reaction rate at 160 °C = 0.061 $\mu\text{mol}/(\text{g}_{\text{cat}} \text{s})$) [4], 1.3 wt% Au/CeO₂ ($T_{90\%} = 250$ °C at SV = 35,000 h⁻¹; toluene reaction rate at 160 °C = 0.029 $\mu\text{mol}/(\text{g}_{\text{cat}} \text{s})$) [22], and 15 wt% Mn/Clinoptilolite–CeO₂ ($T_{90\%} = 320$ °C at SV = 6000 h⁻¹; toluene reaction rate at 160 °C = 0.003 $\mu\text{mol}/(\text{g}_{\text{cat}} \text{s})$) [23], but

was inferior in activity to 0.2 at% Pt/CeO₂-nanorod ($T_{90\%} = 150$ °C at SV = 48,000 mL/(g h); toluene reaction rate at 160 °C = 0.976 $\mu\text{mol}/(\text{g}_{\text{cat}} \text{s})$) [24] and 6.5 wt% Au/meso-Co₃O₄ ($T_{90\%} = 138$ °C at SV = 20,000 mL/(g h) ; toluene reaction rate at 160 °C = 0.956 $\mu\text{mol}/(\text{g}_{\text{cat}} \text{s})$) [25].

In order to investigate catalytic stability of the 0.37Pt–0.16MnO_x/meso-CeO₂ sample, we carried out on-stream toluene combustion at 160 and 180 °C and SV = 40,000 mL/(g h), and the results are shown in Fig. 7. There was no apparent loss in activity within 30 h of on-stream reaction at 160 or 180 °C, demonstrating that the 0.37Pt–0.16MnO_x/meso-CeO₂ sample possessed a good catalytic stability under the adopted conditions.

Since H₂O and CO₂ are the main products in toluene combustion, it is necessary to probe their effects (Fig. 8) on activity of the best-performing 0.37Pt–0.16MnO_x/meso-CeO₂ sample at 180 °C and SV = 40,000 mL/(g h). It is obviously seen that introduction of 1.0–5.0 vol% water vapor to the reaction system did not induce considerable changes in activity (Fig. 8A), which demonstrates that the 0.37Pt–0.16MnO_x/meso-CeO₂ sample exhibited good water-resistant performance. Owing to competitive adsorption of carbon dioxide and toluene molecules on active sites of the sample, toluene conversion decreased from 96 to 88 % in the presence of 5.0 vol% CO₂, but it was slowly recovered after cutting off the provision of CO₂ (Fig. 8B). This result suggests that partial deactivation of 0.37Pt–0.16MnO_x/meso-CeO₂ caused by CO₂ was reversible.

3.3. Low-temperature reducibility

The low-temperature reducibility of a catalyst is important in the low-temperature

removal of VOCs [26]. H₂-TPR technique was employed to measure reducibility of the samples, and their profiles are illustrated in Fig. 9A. For the meso-CeO₂ sample, the peak at 515 °C was owing to reduction of Ce⁴⁺ to Ce³⁺. After doping MnO_x on the surface of meso-CeO₂, the peak at 511 °C originated from reduction of Ce⁴⁺ to Ce³⁺, and the one at 255 °C was ascribable to reduction of MnO₂ and/or Mn₂O₃ to Mn₃O₄. After loading of Pt on the surface of meso-CeO₂, the peak assignable to reduction of Ce⁴⁺ to Ce³⁺ was considerably shifted to a lower temperature (228 °C), which was a result due to promotional effect of the hydrogen chemically adsorbed on the Pt NPs [27]. Hence, loading of Pt NPs could greatly improve low-temperature reducibility of meso-CeO₂. When Pt–MnO_x was loaded on the surface of meso-CeO₂, the reduction band was significantly shifted to a low temperature (100–120 °C), which was owing to reduction of the oxidized Pt²⁺ to Pt⁰ as well as the removal of adsorbed oxygen species. It can be seen from Table 3 that H₂ consumption of the meso-CeO₂ and 0.16MnO_x/meso-CeO₂ samples was 10.3 and 10.6 mmol/g_{cat}, respectively, whereas that (10.9–12.5 mmol/g_{cat}) of the *m*Pt–*n*MnO_x/meso-CeO₂ samples was increased. Based on the surface Ce⁴⁺, Mn³⁺, and Pt²⁺ contents obtained after quantitatively analyzing their XPS spectra, we can see that theoretical H₂ consumption of the meso-CeO₂, 0.16MnO_x/meso-CeO₂, and 0.39Pt/meso-CeO₂ samples was in the range of 14.5–15.0 mmol/g_{cat}, but it increased from 15.2 to 19.6 mmol/g_{cat} when the doped MnO_x content rose from 0.16 to 1.21 wt% (Table S2). Obviously, theoretical H₂ consumption of the samples was higher than their corresponding actual H₂ consumption, which was due to the fact that surface element compositions of the samples were different from their bulk

compositions. Fig. 9B shows the initial H₂ consumption rate as a function of inverse temperature of the samples, from which one can realize that the low-temperature reducibility increased in the order of meso-CeO₂ < 0.16MnO_x/meso-CeO₂ < 0.39Pt/meso-CeO₂ < 0.37Pt–1.21MnO_x/meso-CeO₂ < 0.36Pt–0.78MnO_x/meso-CeO₂ < 0.37Pt–0.16MnO_x/meso-CeO₂, with the 0.37Pt–0.16MnO_x/meso-CeO₂ sample possessing the best low-temperature reducibility (coinciding with its highest catalytic activity for toluene combustion). Therefore, catalytic activity of the sample was closely related to its low-temperature reducibility.

3.4. Surface property

We used the XPS technique to investigate the element compositions, metal oxidation states, and adsorbed oxygen species on the surface of the samples, and their Ce 3d, O 1s, Pt 4f, and Mn 2p_{3/2} XPS spectra are presented in Fig. 10. Two sets of the Ce 3d_{3/2} and Ce 3d_{5/2} signals (Fig. 10A) were recorded: (i) The 3d_{3/2} final states at binding energy (BE) = 901.7, 904.2, 908.8, and 917.3 eV; and (ii) the 3d_{5/2} final states at BE = 882.5, 885.0, 889.9, and 898.5 eV. The components at BE = 885.0 and 904.2 eV were the signals from the surface Ce³⁺ species, while the others originated from the surface Ce⁴⁺ species [28,29]. The result clearly indicates that the Ce on the surface of each sample was present in Ce³⁺ and Ce⁴⁺. The Ce³⁺/Ce⁴⁺ molar ratios (0.25–0.26) of meso-CeO₂ and 0.16MnO_x/meso-CeO₂ were lower than those (0.29–0.34) of 0.39Pt/meso-CeO₂, 0.37Pt–0.16MnO_x/meso-CeO₂, 0.36Pt–0.78MnO_x/meso-CeO₂, and 0.37Pt–1.21MnO_x/meso-CeO₂ (Table 2), with the 0.37Pt–0.16MnO_x/meso-CeO₂ sample possessing the highest Ce³⁺/Ce⁴⁺ molar ratio (0.34). In meso-CeO₂, a higher

Ce^{3+} content means a more amount of oxygen vacancies. It is well known that gas-phase oxygen molecules can be activated at oxygen vacancies to be the active oxygen adspecies, which would be favorable for the combustion of VOCs. Hence, the 0.37Pt–0.16MnO_x/meso-CeO₂ sample performed the best, a result due to its highest oxygen vacancy density. As shown in Fig. 10B, the asymmetrical O 1s spectrum of each sample was decomposed into three components at BE = 529.6, 531.9, and 533.6 eV, corresponding to the surface lattice oxygen (O_{latt}), adsorbed oxygen (O_{ads}), and adsorbed water or carbonate species [30], respectively. As can be seen from Table 2, the 0.37Pt–0.16MnO_x/meso-CeO₂ sample possessed the highest O_{ads}/O_{latt} molar ratio (0.85) among all of the samples, again confirming that a high O_{ads} concentration favored toluene combustion. Illustrated in Fig. 10C are Pt 4f XPS spectra of the 0.39Pt/meso-CeO₂, 0.37Pt–0.16MnO_x/meso-CeO₂, 0.36Pt–0.78MnO_x/meso-CeO₂, and 0.37Pt–1.21MnO_x/meso-CeO₂ samples. The components at BE = 72.8 and 76.1 eV were owing to the surface Pt⁰ species, whereas the ones at BE = 74.2 and 78.1 eV originated from the surface Pt²⁺ species [31]. Usually, the oxidized noble metal can facilitate the improvement in activity of a supported catalyst for VOCs oxidation. As shown in Table 2, the Pt²⁺/Pt⁰ molar ratio (2.6) on the surface of 0.37Pt–0.16MnO_x/meso-CeO₂ was the highest, rendering this sample to show the best catalytic activity for toluene combustion. Fig. 10D presents Mn 2p_{3/2} XPS spectra of the Mn-containing samples. Due to the low doping of MnO_x, intensity of the Mn 2p_{3/2} signal was weak. Each of the Mn 2p_{3/2} spectra was asymmetrical and could be decomposed into two components at BE = 642.1 and 640.6 eV as well a weak satellite

at BE = 644.3 eV, which were ascribed to the surface Mn^{3+} and Mn^{2+} species [32,33], respectively. The surface $\text{Mn}^{2+}/\text{Mn}^{3+}$ molar ratio decreased from 2.5 to 1.7 with the MnO_x loading increased from 0.16 to 1.21 wt% (Table 2), indicating that the surface Mn^{2+} concentration was the highest on the surface of the 0.37Pt–0.16 MnO_x /meso- CeO_2 sample. Previously, we demonstrated that CoO was more active than Co_3O_4 (in which Co^{2+} and Co^{3+} co-existed) for the combustion of *o*-xylene [34]. Similarly, MnO would be more active than MnO_x (in which Mn^{2+} and Mn^{3+} co-existed (Mn 2p_{3/2} XPS results). That is to say, a higher Mn^{2+} concentration on the surface of 0.37Pt–0.16 MnO_x /meso- CeO_2 would favor the combustion of toluene.

Generally speaking, O_{ads} species (for example, O_2^- , O_2^{2-} or O^-) have an important role to play in the reduction–oxidation reactions [35]. A higher O_{ads} concentration is usually favorable for the combustion of VOCs. The toluene reaction rate (normalized per gram of noble metal), TOF_{Pt} (normalized per mole of Pt) and TOF_{Mn} (normalized per mole of Mn) at 160 °C as a function of surface $\text{O}_{\text{ads}}/\text{O}_{\text{latt}}$ molar ratio of the samples are shown in Fig. 11. Obviously, the toluene reaction rate and TOF_{Pt} or TOF_{Mn} at 160 °C increased with the rise in $\text{O}_{\text{ads}}/\text{O}_{\text{latt}}$ molar ratio. The results demonstrate that catalytic performance was closely related to the O_{ads} species concentration. Moreover, PtO and MnO was the main active sites for toluene activation, and higher surface PtO and MnO concentrations would render the catalyst to show a better activity. Based on the O_{ads} , PtO, and MnO species concentrations on the sample surface (Table 2), it is understandable that the 0.37Pt–0.16 MnO_x /meso- CeO_2 sample performed the best in toluene combustion.

3.5. O₂-TPD, toluene-TPD, and in situ DRIFTS

To probe oxygen and toluene adsorption ability, we used the O₂- and toluene-TPD techniques to determine desorption behaviors of oxygen and toluene from the 0.39Pt/meso-CeO₂ and *m*Pt-*n*MnO_{*x*}/meso-CeO₂ samples. As can be seen from the O₂-TPD profiles (Fig. 12), the first peak at low temperature (< 200 °C) originated from desorption of the chemisorbed oxygen species as well as decomposition of surface PtO, the second one between 200–400 °C was due to desorption of the oxygen from the MnO_{*x*} (Mn²⁺_{1-*y*}Mn³⁺_{*y*}O_{*x*} → Mn²⁺O), while the last one at high temperature (> 500 °C) corresponded to desorption of the lattice oxygen from meso-CeO₂ [36]. After quantitative analysis on the peaks in O₂-TPD profiles of the samples, one can see that the amount (0.97 mmol/g_{cat}) of the chemisorbed oxygen species as well as the surface oxygen species due to PtO decomposition (the first peak) was the highest on 0.37Pt–0.16MnO_{*x*}/meso-CeO₂, although the total oxygen desorption below 400 °C increased with the rise in MnO_{*x*} doping (Table 3), which might be a result owing to the increased Mn³⁺ concentration in the enhanced MnO_{*x*}-doped sample. In general, toluene adsorption ability is one of the factors influencing activity of a catalyst. As shown in the toluene-TPD profiles (Fig. 13), each sample exhibited a toluene desorption peak centered at 75–83 °C, assignable to desorption of the physically and/or weakly chemisorbed toluene; and toluene desorption also increased with the rise in MnO_{*x*} doping (Table 3). This result suggests that doping of MnO_{*x*} was beneficial for the enhancement in toluene adsorption. The temperature (ca. 75 °C) of the desorption peak over the 0.39Pt/meso-CeO₂ or 0.37Pt–0.16MnO_{*x*}/meso-CeO₂ sample was lower than that (ca. 83 °C) over the 0.37Pt–0.78MnO_{*x*}/meso-CeO₂ or 0.37Pt–1.21MnO_{*x*}/meso-CeO₂ sample, indicating that adsorption of toluene on the latter samples was stronger than that on the former samples. Since the best catalytic activity was achieved over

0.37Pt–0.16MnO_x/meso-CeO₂ with the lowest toluene adsorption (33.8 μmol/g_{cat}), whereas 0.37Pt–1.21MnO_x/meso-CeO₂ with the highest toluene adsorption (72.8 μmol/g_{cat}) showed the lowest catalytic activity among the *m*Pt–*n*MnO_x/meso-CeO₂ samples, it can be reasonably deduced that toluene adsorption was not responsible for catalytic activity of the *m*Pt–*n*MnO_x/meso-CeO₂ samples. In other words, toluene combustion might undergo via the interaction of gas-phase toluene with the O_{ads} species to produce CO₂ and H₂O (i.e., the Eley–Rideal reaction mechanism might dominate the combustion of toluene) or there were other factors (e.g., surface O_{ads} and Mn²⁺ species concentrations and low-temperature reducibility) influence toluene combustion. Based on the above characterization results, we can realize that the enhanced adsorbed oxygen and Mn²⁺ species concentration and improved low-temperature reducibility induced by loading of Pt and MnO_x were responsible for the good toluene combustion performance of 0.37Pt–0.16MnO_x/meso-CeO₂.

In order to identify the intermediate species during toluene combustion, we used the in situ DRIFTS technique to monitor the possibly formed intermediates on 0.39Pt/meso-CeO₂ and 0.37Pt–0.16MnO_x/meso-CeO₂. The in situ DRIFTS spectra of the two samples at different temperatures are shown in Fig. 14, and their absorption band assignments can be seen from Table S3. The absorption bands at 1494 and 1602 cm⁻¹ originated from ring vibrations of toluene [37,38], the one at 2972–3072 cm⁻¹ was carbon–hydrogen stretching vibration of the aromatic rings in toluene, and the one at 2925 cm⁻¹ was the carbon–hydrogen stretching vibration of the alkyl group in toluene [39]. By comparing band intensity of the two samples, we can realize that a higher amount of aromatic ring species and a lower amount of alkyl groups were formed over

the 0.37Pt–0.16MnO_x/meso-CeO₂ sample at the same temperature. It can be reasonably deduced that the alkyl group in toluene was first oxidized and the aromatic ring was then oxidized. When the temperature increased, the two bands at 2348 (belonging to CO₂) and 3684 cm⁻¹ (belonging to H₂O) appeared over both samples. This result demonstrates that the aromatic ring was further oxidized to carbon dioxide and water at high temperatures. In addition, benzyl alcohol (1180–1310 cm⁻¹), benzoic acid (1531 and 1452 cm⁻¹), and maleic anhydride (1811–1966 cm⁻¹) were also detected as intermediates [40,41]. Therefore, toluene combustion might proceed according to the following steps: toluene → benzyl alcohol and benzoic acid → maleic anhydride → carbon dioxide and water.

4. Conclusions

The PtMn_y intermetallic NCs were synthesized via the PVP-assisted EG reduction route. Loading of PtMn_y NCs on the surface of meso-CeO₂ (derived by the KIT-6-templating method) and after calcination at 500 °C in air led to generation of the *m*Pt–*n*MnO_x/meso-CeO₂ catalysts. All of the samples were cubic in crystal structure and displayed an ordered mesoporous architecture with surface areas of 95–108 m²/g. Loading of Pt and MnO_x resulted in improved low-temperature reducibility and increased O_{ads} and Mn²⁺ species concentration (which were beneficial for toluene combustion), and doping of MnO_x also enhanced toluene adsorption ability. Among all of the samples, 0.37Pt–0.16MnO_x/meso-CeO₂ performed the best for toluene combustion ($T_{50\%} = 162$ °C and $T_{90\%} = 171$ °C at SV = 40,000 mL/(g h)). Moreover, the 0.37Pt–0.16MnO_x/meso-CeO₂ sample possessed low activation energy and good

thermal stability and water-resistant performance. The competitive adsorption of CO₂ and toluene molecules on the surface of 0.37Pt–0.16MnO_x/meso-CeO₂ made CO₂ introduction exert a negative effect on toluene combustion, but its induced partial deactivation was reversible. Toluene combustion might undergo via a sequence of toluene → benzyl alcohol and benzoic acid → maleic anhydride → carbon dioxide and water.

Credit author statement

Mr. Wenbo Pei prepared the catalysts, evaluated the activities, and made characterization of XRD, SEM, TEM, HAADF–STEM, BET, O₂-TPD, and H₂-TPR; Prof. Jiguang Deng and Lin Jing examined the effect of treatment temperature on activity of the typical samples; Mr. Kunfeng Zhang, Zhiqian Hou, Zhuo Han and Ali Rastegarpanah did the XPS and FT-IR characterization and examined the effects of SV, H₂O, CO₂, and SO₂; Prof. Hongxing Dai and Dr. Yuxi Liu was responsible for the whole work.

Acknowledgements

This work was supported by the NSF of China (21677004, 21876006, and 21976009), National Natural Science Committee of China–Liaoning Provincial People's Government Joint Fund (U1908204), and Foundation on the Creative Research Team Construction Promotion Project of Beijing Municipal Institutions (IDHT20190503), and Natural Science Foundation of Beijing Municipal Commission of Education (SQKM201710005004).

Appendix A. Supplementary Data

Supplementary data associated with this article can be found, in the online version, at

<http://dx.doi.org/10.1016/j.apcata.2020.XX.XXX>.

References

- [1] R.S. Drago, K. Jurczyk, D.J. Singh, V. Young, Low-temperature deep oxidation of hydrocarbons by metal oxides supported on carbonaceous materials, *Appl. Catal. B* 6 (1995) 155–168.
- [2] C.Y. Ma, Z. Mu, J.J. Li, Y.G. Jin, J. Cheng, G.Q. Lu, Z.P. Hao, S.Z. Qiao, Mesoporous Co_3O_4 and $\text{Au}/\text{Co}_3\text{O}_4$ catalysts for low-temperature oxidation of trace ethylene, *J. Am. Chem. Soc.* 132 (2010) 2608–2613.
- [3] Y.F. Wang, C.B. Zhang, F.D. Liu, H. He, Well-dispersed palladium supported on ordered mesoporous Co_3O_4 for catalytic oxidation of *o*-xylene, *Appl. Catal. B* 142–143 (2013) 72–79.
- [4] H.G. Yang, J.G. Deng, Y.X. Liu, S.H. Xie, Z.X. Wu, H.X. Dai, Preparation and catalytic performance of Ag, Au, Pd or Pt nanoparticles supported on 3DOM $\text{CeO}_2\text{-Al}_2\text{O}_3$ for toluene oxidation, *J. Mol. Catal. A* 414 (2016) 9–18.
- [5] R.J. Farrauto, J.K. Lampert, M.C. Hobson, E. Waterman, Thermal decomposition and reformation of PdO catalysts: support effects, *Appl. Catal. B* 6 (1995) 263–270.
- [6] M. Comotti, W.C. Li, B. Spliethoff, S. Ferdi, Support effect in high activity gold catalysts for CO, *J. Am. Chem. Soc.* 128 (2006) 917–924.
- [7] M.Y. Kim, T. Masui, N. Imanaka, Complete oxidation of toluene on refractory $\text{La}_{1-x}\text{Ca}_x\text{CoO}_{3-x/2}/\text{CeO}_2\text{-ZrO}_2\text{-ZnO}$ catalysts, *Catal. Sci. Technol.* 4 (2014) 321–324.
- [8] H. Huang, Q.G. Dai, X.Y. Wang, Morphology effect of Ru/CeO_2 catalysts for the

- catalytic combustion of chlorobenzene, *Appl. Catal. B* 158–159 (2014) 96–105.
- [9] Y. Grin, *Comprehensive Inorganic Chemistry II-Vol. 2* (J. Reedijk, K. Poeppelmeier, Eds.), Oxford: Elsevier, 2013, pp. 359–373.
- [10] M. Armbrüster, R. Schlögl, Y. Grin, Intermetallic compounds in heterogeneous catalysis—a quickly developing field, *Sci. Technol. Adv. Mater.* 15 (2014) 034803.
- [11] M. Armbrüster, G. Wowsnick, M. Friedrich, M. Heggen, R. Cardoso-Gil, Synthesis and catalytic properties of nanoparticulate intermetallic Ga–Pd compounds, *J. Am. Chem. Soc.* 133 (2011) 9112–9118.
- [12] J. Osswald, K. Kovnir, M. Armbrüster, R. Giedigkeit, R.E. Jentoft, U. Wild, Y. Grin, R. Schlögl, Palladium–gallium intermetallic compounds for the selective hydrogenation of acetylene: Part II: Surface characterization and catalytic performance, *J. Catal.* 258 (2008) 219–227.
- [13] J.J. Willis, E.D. Goodman, L.H. Wu, A.R. Riscoe, P. Martins, C.J. Tassone, M. Cargnello, Systematic identification of promoters for methane oxidation catalysts using size- and composition-controlled Pd-based bimetallic nanocrystals, *J. Am. Chem. Soc.* 139 (2017) 11989–11997.
- [14] S.H. Xie, J.G. Deng, S.M. Zang, H.G. Yang, G.S. Guo, H. Arandian, H.X. Dai, Au–Pd/3DOM Co_3O_4 : Highly active and stable nanocatalysts for toluene oxidation, *J. Catal.* 322 (2015) 38–48.
- [15] J.M. Yan, X.B. Zhang, T. Akita, M. Haruta, Q. Xu, One-step seeding growth of magnetically recyclable Au@Co core-shell nanoparticles: highly efficient catalyst for hydrolytic dehydrogenation of ammonia borane, *J. Am. Chem. Soc.* 132 (2010)

5326–5327.

- [16] S.F. Ho, A. Mendoza-Garcia, S. Guo, K. He, D. Su, S. Liu, O. Metin, S.H. Sun, A facile route to monodisperse MPd (M = Co or Cu) alloy nanoparticles and their catalysis for electrooxidation of formic acid, *Nanoscale* 6 (2014) 6970–6973.
- [17] Y. Jiang, S.H. Xie, H.G. Yang, J.G. Deng, Y.X. Liu, H.X. Dai, Mn₃O₄–Au/3DOM La_{0.6}Sr_{0.4}CoO₃: High-performance catalysts for toluene oxidation, *Catal. Today* 281 (2017) 437–446.
- [18] K. Yang, Y.X. Liu, J.G. Deng, X.T. Zhao, J. Yang, Z. Han, Z.Q. Hou, H.X. Dai, Three-dimensionally ordered mesoporous iron oxide-supported single-atom platinum: Highly active catalysts for benzene combustion, *Appl. Catal. B* 244 (2019) 650–659.
- [19] Z. Han, Y.X. Liu, J.G. Deng, S.H. Xie, Z.Q. Hou, X.T. Zhao, K.F. Zhang, J. Yang, H.X. Dai, Preparation and catalytic performance of Co₃O₄–MnO₂ for *o*-xylene combustion, *Catal. Today* 327 (2019) 246–253.
- [20] F. Kleita, S.H. Choi, R. Ryoo, Cubic *Ia3d* large mesoporous silica: Synthesis and replication to platinum nanowires, carbon nanorods and carbon nanotubes, *Chem. Commun.* (2003) 2136–2137.
- [21] K. Bendahou, L. Cherif, S. Siffert, H.L. Tidahy, H. Benaïssa, A. Aboukaïs, The effect of the use of lanthanum-doped mesoporous SBA-15 on the performance of Pt/SBA-15 and Pd/SBA-15 catalysts for total oxidation of toluene, *Appl. Catal. A* 351 (2008) 82–87.
- [22] M. Ousmanea, L.F. Liotta d, G. Di Carloe, G. Pantaleo, A.M. Venezia d, G.

- Deganelloc, L. Retailleau, A. Boreavea, A. Giroir-Fendler, Supported Au catalysts for low-temperature abatement of propene and toluene, as model VOCs: Support effect, *Appl. Catal. B* 101 (2011) 629–637.
- [23] L. Yosefi, M. Haghghi, S. Allahyari, R. Shokrani, S. Ashkriz, Abatement of toluene from polluted air over Mn/Clinoptilolite–CeO₂ nanopowder: Impregnation vs. ultrasound assisted synthesis with various Mn-loading, *Adv. Powder Technol.* 26 (2015) 602–611.
- [24] R.S. Peng, X.B. Sun, S.J. Li, L.M. Chen, M.L. Fu, J.L. Wu, D.Q. Ye, Shape effect of Pt/CeO₂ catalysts on the catalytic oxidation of toluene, *Chem. Eng. J.* 306 (2016) 1234–1246.
- [25] Y.X. Liu, H.X. Dai, J.G. Deng, S.H. Xie, H.G. Yang, W. Tan, W. Han, Y. Jiang, G.S. Guo, Mesoporous Co₃O₄-supported gold nanocatalysts: Highly active for the oxidation of carbon monoxide, benzene, toluene, and *o*-xylene, *J. Catal.* 309 (2014) 408–418.
- [26] J.J. Kong, G.Y. Li, M.C. Wen, J.Y. Chen, H.L. Liu, T.C. An, The synergic degradation mechanism and photothermocatalytic mineralization of typical VOCs over PtCu/CeO₂ ordered porous catalysts under simulated solar irradiation, *J. Catal.* 370 (2019) 88–96.
- [27] S.H. Xie, Y.X. Liu, J.G. Deng, S.M. Zang, Z.H. Zhang, H. Arandiyani, H.X. Dai, Efficient removal of methane over cobalt-monoxide-doped AuPd nanocatalysts, *Environ. Sci. Technol.* 51 (2017) 2271–2279.
- [28] Y.Z. Li, Q. Sun, M. Kong, W.Q. Shi, J.C. Huang, J.W. Tang, X.J. Zha, Coupling

- oxygen ion conduction to photocatalysis in mesoporous nanorod-like ceria significantly improves photocatalytic efficiency, *J. Phys. Chem. C* 115 (2011) 14050–14057.
- [29] Z.P. Zhang, L.Q. Chen, Z.B. Li, P.Y. Li, F.L. Yuan, X.Y. Niu, Y.J. Zhu, Activity and SO₂ resistance of amorphous CeTiO_x catalysts for the selective catalytic reduction of NO with NH₃: in situ DRIFT studies, *Catal. Sci. Technol.* 6 (2016) 7151–7162.
- [30] S.H. Xie, Y.X. Liu, J.G. Deng, X.T. Zhao, J. Yang, K.F. Zhang, Z. Han, H.X. Dai, Three-dimensionally ordered macroporous CeO₂-supported Pd@Co nanoparticles: Highly active catalysts for methane oxidation, *J. Catal.* 342 (2016) 17–26.
- [31] Z.B. Wu, Z.Y. Sheng, Y. Liu, H.Q. Wang, J.S. Mo, Deactivation mechanism of PtO_x/TiO₂ photocatalyst towards the oxidation of NO in gas phase, *J. Hazard. Mater.* 185 (2011) 1053–1058.
- [32] L.L. Zhao, Z.P. Zhang, Y.S. Liu, X.S. Leng, T.R. Zhang, F.L. Yuan, X.Y. Niu, Y.J. Zhu, Synthesis of CeMnO_x hollow microsphere with hierarchical structure and its excellent catalytic performance for toluene combustion, *Appl. Catal. B* 245 (2019) 502–512.
- [33] M. Piumetti, D. Fino, N. Russo, Mesoporous manganese oxides prepared by solution combustion synthesis as catalysts for the total oxidation of VOCs, *Appl. Catal. B* 163 (2015) 277–287.
- [34] S.H. Xie, YX. Liu, J.G. Deng, J. Yang, X.T. Zhao, Z. Han, K.F. Zhang, H.X. Dai, Insights into the active sites of ordered mesoporous cobalt oxide catalysts for the

- total oxidation of *o*-xylene, *J. Catal.* 352 (2017) 282–292.
- [35] Y. Liu, B.C. Liu, Q. Wang, C.Y. Li, W.T. Hu, Y.X. Liu, P. Jing, W.Z. Zhao, J. Zhang, Three-dimensionally ordered macroporous Au/CeO₂-Co₃O₄ catalysts with mesoporous walls for enhanced CO preferential oxidation in H₂-rich gases, *J. Catal.* 296 (2012) 65–76.
- [36] Z.Y. Hou, J. Feng, T. Lin, H.L. Zhang, X.Y. Zhou, Y.Q. Chen, The performance of manganese based catalysts with Ce_{0.65}Zr_{0.35}O₂ as support for catalytic oxidation of toluene, *Appl. Surf. Sci.* 434 (2018) 82–90.
- [37] Y.N. Liao, X. Zhang, R.S. Peng, M.Q. Zhao, D.Q. Ye, Catalytic properties of manganese oxide polyhedra with hollow and solid morphologies in toluene removal, *Appl. Surf. Sci.* 405 (2017) 20–28.
- [38] S. Besselmann, E. Löffler, M. Muhler, On the role of monomeric vanadyl species in toluene adsorption and oxidation on V₂O₅/TiO₂ catalysts: a Raman and in situ DRIFTS study, *J. Mol. Catal. A* 162 (2000) 401–411.
- [39] S. Zhao, F.Y. Hu, J.H. Li, Hierarchical core-shell Al₂O₃@Pd-CoAlO microspheres for low-temperature toluene combustion, *ACS Catal.* 6 (2016) 3433–3441.
- [40] F. Rainone, D.A. Bulushev, L. Kiwi-Minsker, A. Renken, DRIFTS and transient-response study of vanadia/titania catalysts during toluene partial oxidation, *Phys. Chem. Chem. Phys.* 5 (2003) 4445–4449.
- [41] J. Li, H. Na, X. Zeng, T. Zhu, Z. Liu, In situ DRIFTS investigation for the oxidation of toluene by ozone over Mn/HZSM-5, Ag/HZSM-5 and Mn-Ag/HZSM-5 catalysts, *Appl. Surf. Sci.* 311 (2014) 690–696.

Table 1. BET surface areas, pore volumes, average pore diameters, average crystallite sizes (D_{support}), actual Pt or MnO_x contents, and Mn/Pt molar ratios of the samples.

Table 2. Catalytic activities at $\text{SV} = 40,000 \text{ mL}/(\text{g h})$, TOFs and toluene combustion rates at $160 \text{ }^\circ\text{C}$, apparent activation energies (E_a), and surface element compositions of the samples.

Table 3. H_2 consumption, oxygen desorption, and toluene desorption calculated by quantitatively analyzing the H_2 -TPR, O_2 -TPD, and toluene-TPD profiles of the samples.

Fig. 1. (A) Wide- and (B) small-angle XRD patterns of (a) meso- CeO_2 , (b) $0.37\text{Pt}-0.16\text{MnO}_x/\text{meso-CeO}_2$, (c) $0.36\text{Pt}-0.78\text{MnO}_x/\text{meso-CeO}_2$, (d) $0.37\text{Pt}-1.21\text{MnO}_x/\text{meso-CeO}_2$, (e) $0.39\text{Pt}/\text{meso-CeO}_2$, and (f) $0.16\text{MnO}_x/\text{meso-CeO}_2$.

Fig. 2. (A) Nitrogen adsorption-desorption isotherms and (B) pore-size distributions of (a) meso- CeO_2 , (b) $0.37\text{Pt}-0.16\text{MnO}_x/\text{meso-CeO}_2$, (c) $0.36\text{Pt}-0.78\text{MnO}_x/\text{meso-CeO}_2$, (d) $0.37\text{Pt}-1.21\text{MnO}_x/\text{meso-CeO}_2$, (e) $0.39\text{Pt}/\text{meso-CeO}_2$, and (f) $0.16\text{MnO}_x/\text{meso-CeO}_2$.

Fig. 3. TEM images of (a, b) meso- CeO_2 , (c, d) $0.39\text{Pt}/\text{meso-CeO}_2$, (e, f) $0.37\text{Pt}-0.16\text{MnO}_x/\text{meso-CeO}_2$, and (g, h) $0.16\text{MnO}_x/\text{meso-CeO}_2$.

Fig. 4. HADDF-STEM image and elemental mappings of the $0.37\text{Pt}-0.16\text{MnO}_x/\text{meso-CeO}_2$ sample.

Fig. 5. (a, b) TEM images and (c) particle-size distribution of $\text{PtMn}_{1.5}$ NPs.

Fig. 6. (A) Toluene conversion as a function of reaction temperature, (B) reaction rate normalized per gram of catalyst, and (C) Arrhenius plots of (a) meso- CeO_2 , (b)

0.37Pt–0.16MnO_x/meso-CeO₂, (c) 0.36Pt–0.78MnO_x/meso-CeO₂, (d) 0.37Pt–1.21MnO_x/meso-CeO₂, (e) 0.39 Pt/meso-CeO₂, and (f) 0.16MnO_x/meso-CeO₂ at SV = 40,000 mL/(g h).

Fig. 7. Toluene conversion as a function of on-stream reaction time over 0.37Pt–0.16MnO_x/meso-CeO₂ at 160 and 180 °C at SV = 40,000 mL/(g h), respectively.

Fig. 8. Effects of (A) H₂O and (B) CO₂ on catalytic activity of 0.37Pt–0.16MnO_x/meso-CeO₂ at 180 °C and SV = 40,000 mL/(g h).

Fig. 9. (A) H₂-TPR profiles and (B) initial H₂ consumption rate as a function of inverse temperature of the samples.

Fig. 10. (A) Ce 3d, (B) O 1s, (C) Pt 4f, and (D) Mn 2p_{3/2} XPS spectra of (a) meso-CeO₂, (b) 0.16MnO_x/meso-CeO₂, (c) 0.39Pt/meso-CeO₂, (d) 0.37Pt–0.16MnO_x/meso-CeO₂, (e) 0.36Pt–0.78MnO_x/meso-CeO₂, and (f) 0.37Pt–1.21MnO_x/meso-CeO₂.

Fig. 11. O₂-TPD profiles of (a) 0.39Pt/meso-CeO₂ (b) 0.37Pt–0.16MnO_x/meso-CeO₂, (c) 0.36Pt–0.78MnO_x/meso-CeO₂, and (d) 0.37Pt–1.21MnO_x/meso-CeO₂.

Fig. 12. (A) Toluene reaction rate versus O_{ads}/O_{latt} molar ratio, (B) TOF_{Pt} versus O_{ads}/O_{latt} molar ratio, (C) TOF_{Mn} versus O_{ads}/O_{latt} molar ratio of the samples for toluene combustion at 160 °C and SV = 40,000 mL/(g h).

Fig. 13. Toluene-TPD profiles of the samples.

Fig. 14. In situ DRIFTS spectra of (A, B) 0.39Pt/meso-CeO₂ and (C, D) 0.37Pt–0.16MnO_x/meso-CeO₂ during toluene combustion at different temperatures (reaction conditions: 1000 ppm toluene + 20 vol% O₂ + N₂ (balance); SV = 40,000 mL/(g h)).

Journal Pre-proof

Table 1. BET surface areas, pore volumes, average pore diameters, average crystallite sizes (D_{support}), actual Pt or MnO_x contents, and Mn/Pt molar ratios of the samples.

Sample	BET surface area ^a (m ² /g)	Pore volume ^a (cm ³ /g)	Average pore diameter ^a (nm)	D_{support} (nm) ^b	Actual Pt content ^c (wt%)	Actual MnO_x content ^c (wt%)	Mn/Pt molar ratio
meso-CeO ₂	107.9	0.22	4.0	10.0	–	–	–
0.16MnO _x /meso-CeO ₂	95.4	0.19	4.0	10.0	–	0.16	–
0.39Pt/meso-CeO ₂	99.1	0.19	4.0	10.0	0.39	–	–
0.37Pt–0.16MnO _x /meso-CeO ₂	107.1	0.19	4.0	10.0	0.37	0.16	1.5
0.36Pt–0.78MnO _x /meso-CeO ₂	104.5	0.20	4.0	10.0	0.36	0.78	7.7
0.37Pt–1.21MnO _x /meso-CeO ₂	103.6	0.19	4.0	10.0	0.37	1.21	11.6

^a Data were determined by the BET results;

^b Data were obtained according to the Scherrer equation using the FWHM of the (111) line of CeO₂ in the XRD patterns;

^c Data were determined by the ICP–AES technique.

^a Data were obtained by quantitatively analyzing the peaks in XPS spectra of the samples.

Journal Pre-proof

Table 3. H₂ consumption, oxygen desorption, and toluene desorption calculated by quantitatively analyzing the H₂-TPR, O₂-TPD, and toluene-TPD profiles of the samples.

Sample	H ₂ consumption (mmol/g _{cat})	Oxygen desorption below 400 °C (mmol/g _{cat})			Toluene desorption (μmol/g _{cat})
		1 st peak	2 nd peak	Total	
0.16MnO _x /meso-CeO ₂	10.5	–	–	–	–
0.39Pt/meso-CeO ₂	10.9	0.74	–	0.74	21.5
0.37Pt–0.16MnO _x /meso-CeO ₂	11.4	0.97	1.42	2.39	33.8
0.36Pt–0.78MnO _x /meso-CeO ₂	11.8	0.66	2.46	3.12	53.6
0.37Pt–1.21MnO _x /meso-CeO ₂	12.5	0.63	3.00	3.63	72.8

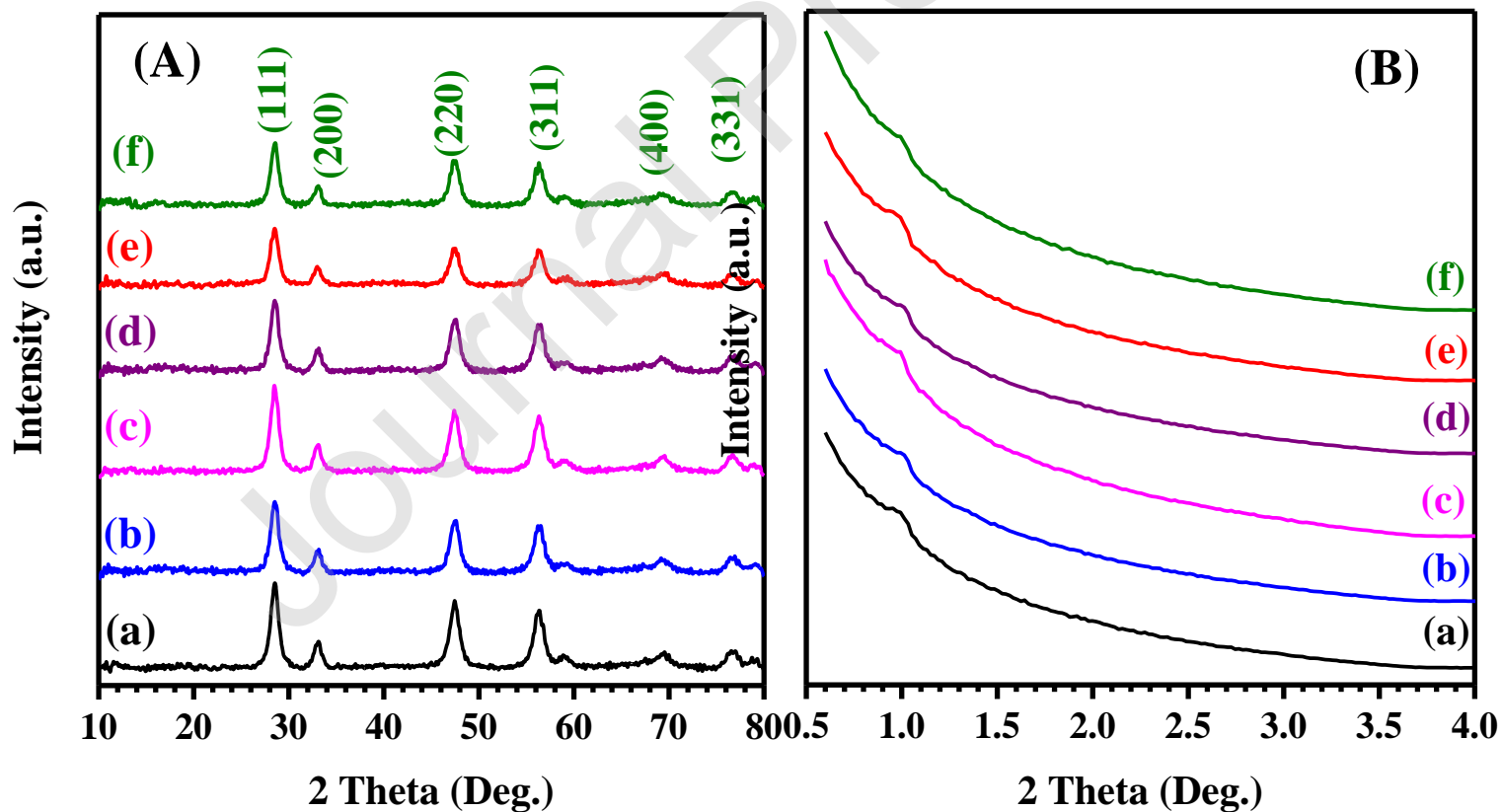


Fig. 1. (A) Wide- and (B) small-angle XRD patterns of (a) meso-CeO₂, (b) 0.37Pt–0.16MnO_x/meso-CeO₂, (c) 0.36Pt–0.78MnO_x/meso-CeO₂, (d) 0.37Pt–1.21MnO_x/meso-CeO₂, (e) 0.39Pt/meso-CeO₂, and (f) 0.16MnO_x/meso-CeO₂.

Journal Pre-proof

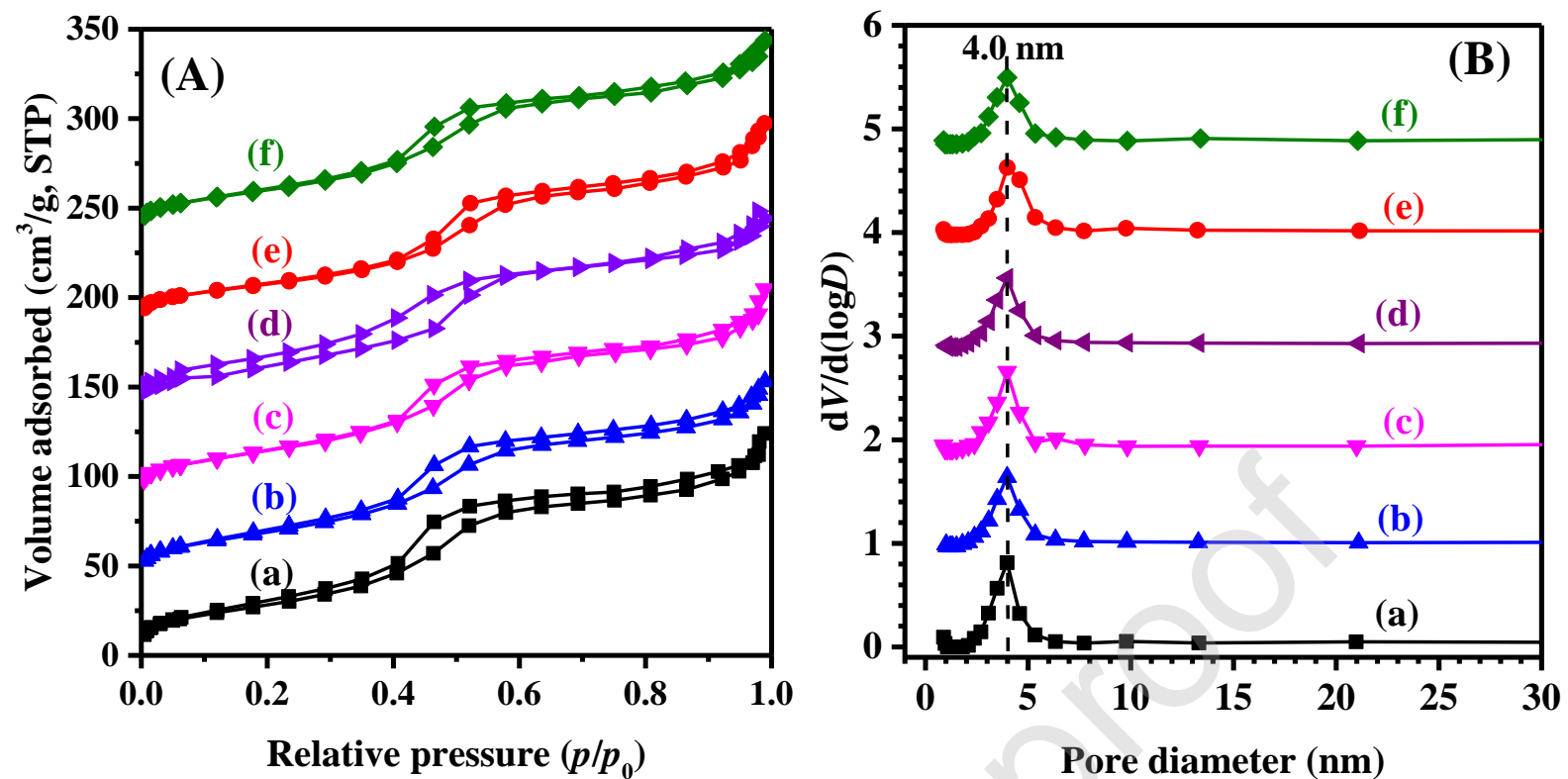


Fig. 2. (A) Nitrogen adsorption–desorption isotherms and (B) pore-size distributions of (a) meso-CeO₂, (b) 0.37Pt–0.16MnO_x/meso-CeO₂, (c) 0.36Pt–0.78MnO_x/meso-CeO₂, (d) 0.37Pt–1.21MnO_x/meso-CeO₂, (e) 0.39Pt/meso-CeO₂, and (f) 0.16MnO_x/meso-

CeO₂.

Journal Pre-proof

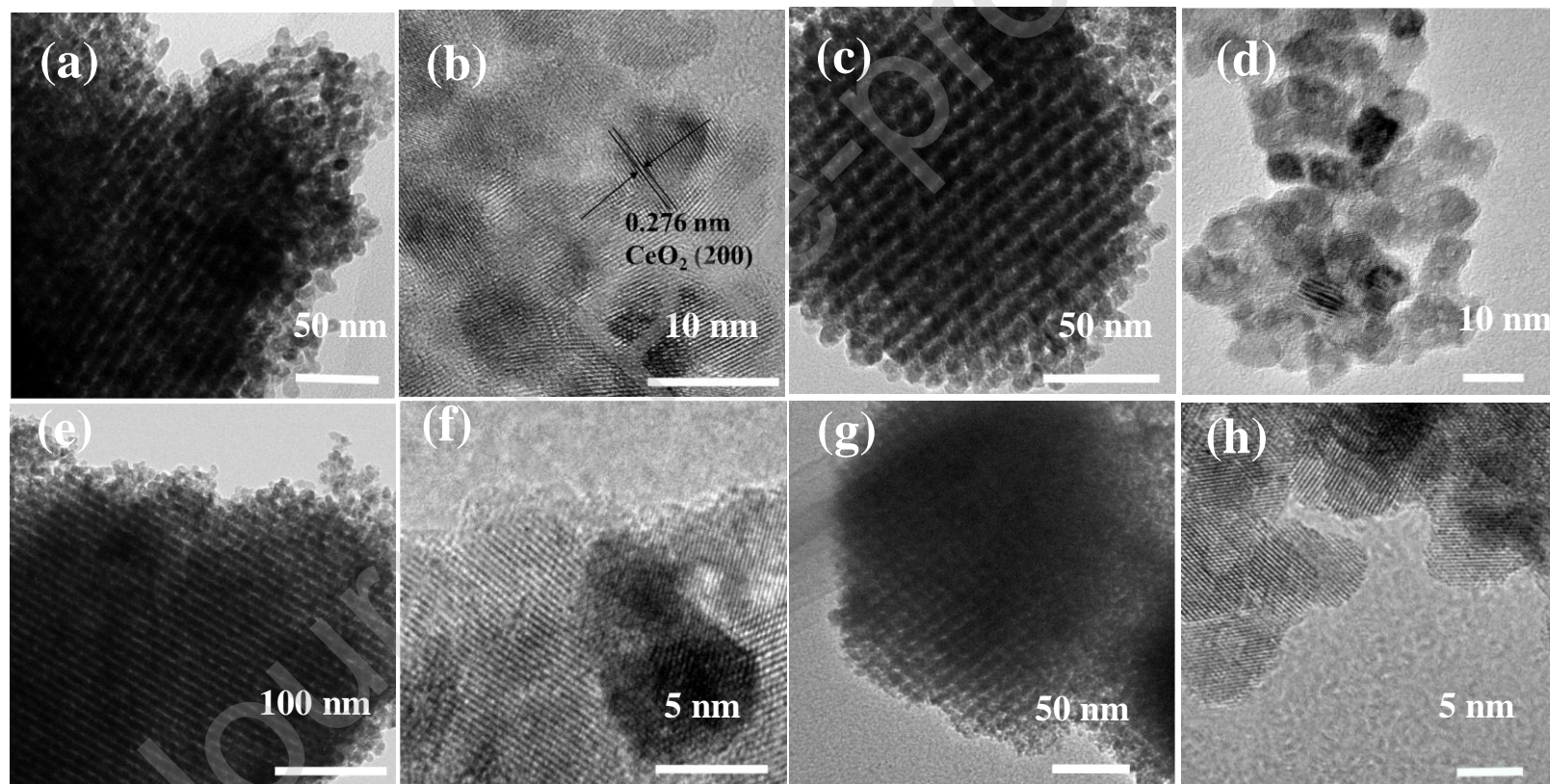


Fig. 3. TEM images of (a, b) meso-CeO₂, (c, d) 0.39Pt/meso-CeO₂, (e, f) 0.37Pt-0.16MnO_x/meso-CeO₂, and (g, h) 0.16MnO_x/meso-CeO₂.

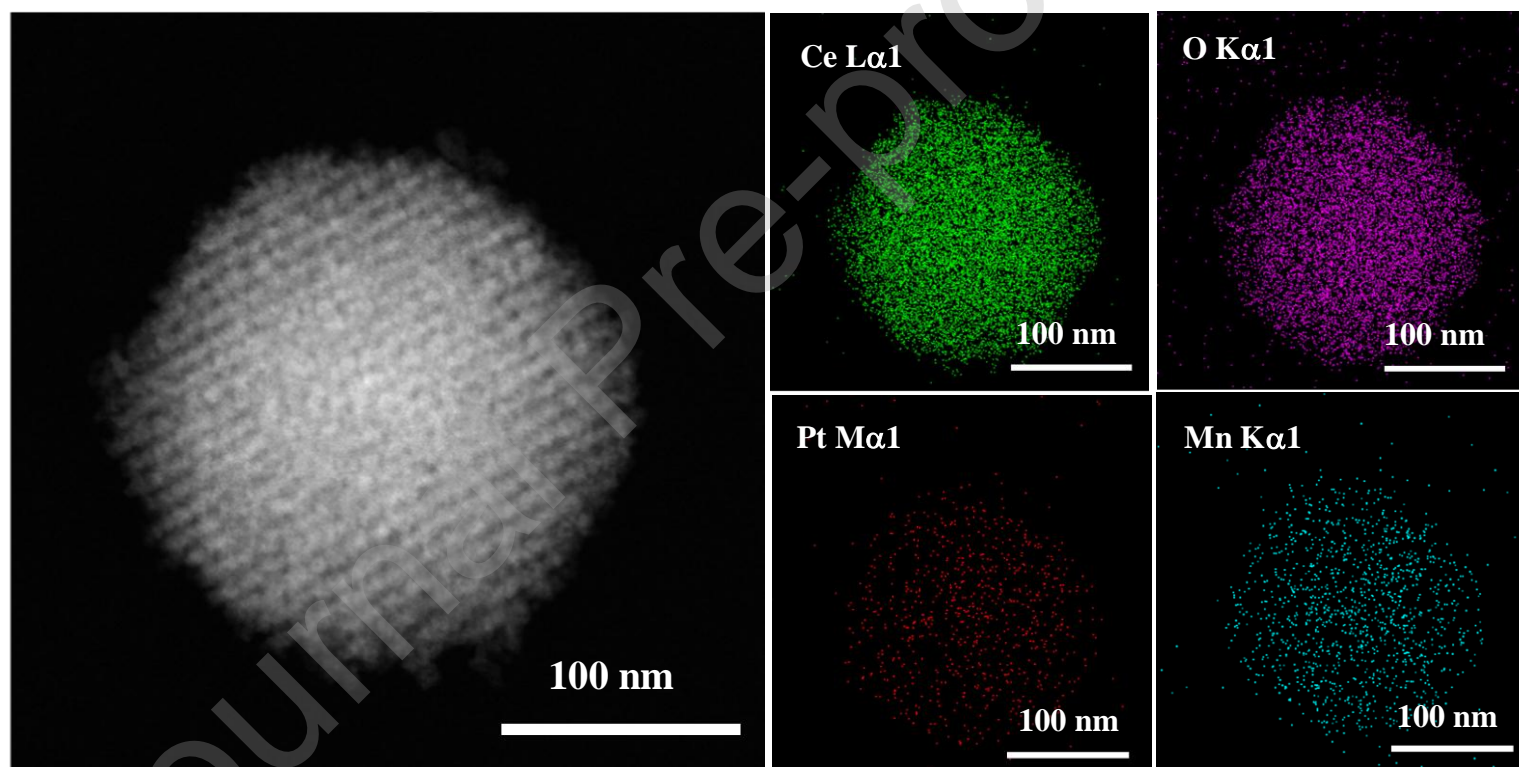


Fig. 4. HADF-STEM image and elemental mappings of the 0.37Pt-0.16MnO_x/meso-CeO₂ sample.

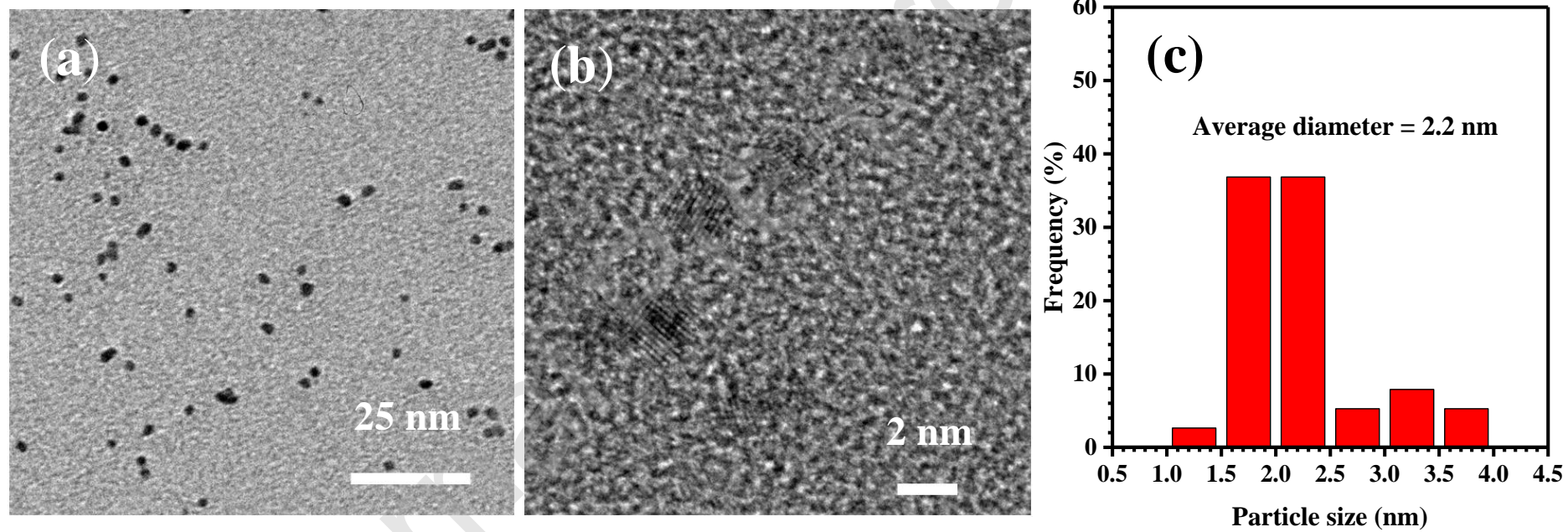
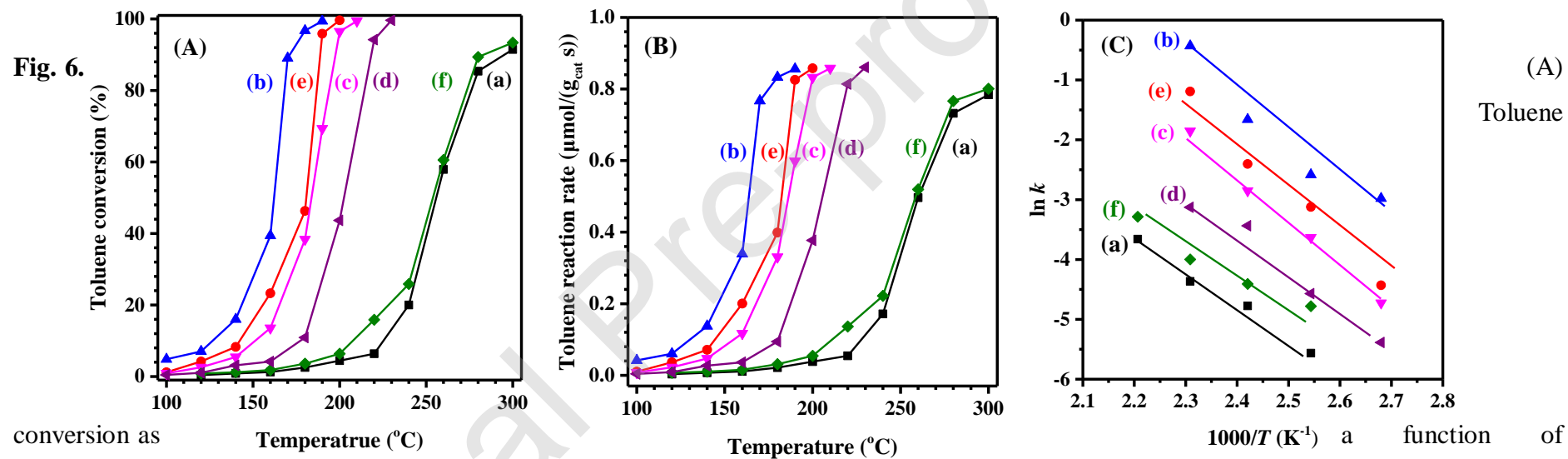


Fig. 5. (a, b) TEM images and (c) particle-size distribution of PtMn_{1.5} NPs.



conversion as a function of reaction temperature, (B) reaction rate normalized per gram of catalyst, and (C) Arrhenius plots of (a) meso-CeO₂, (b) 0.37Pt-0.16MnO_x/meso-CeO₂, (c) 0.36Pt-0.78MnO_x/meso-CeO₂, (d) 0.37Pt-1.21MnO_x/meso-CeO₂, (e) 0.39 Pt/meso-CeO₂, and (f) 0.16MnO_x/meso-CeO₂ at SV = 40,000 mL/(g h).

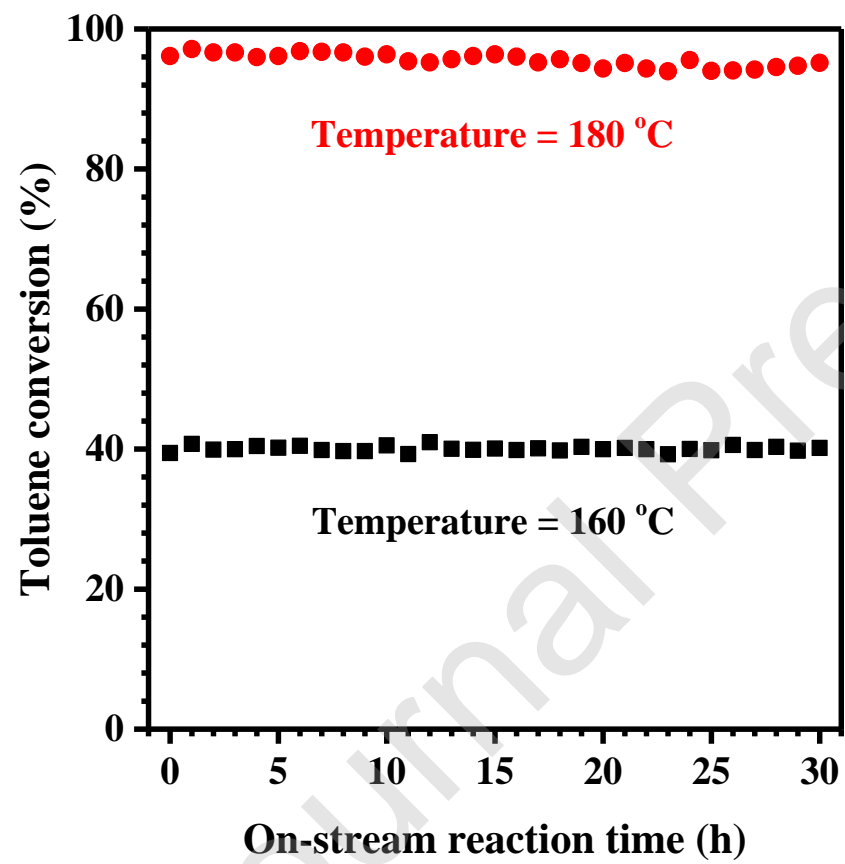


Fig. 7. Toluene conversion as a function of on-stream reaction time over 0.37Pt–0.16MnO_x/meso-CeO₂ at 160 and 180 °C at SV = 40,000 mL/(g h), respectively.

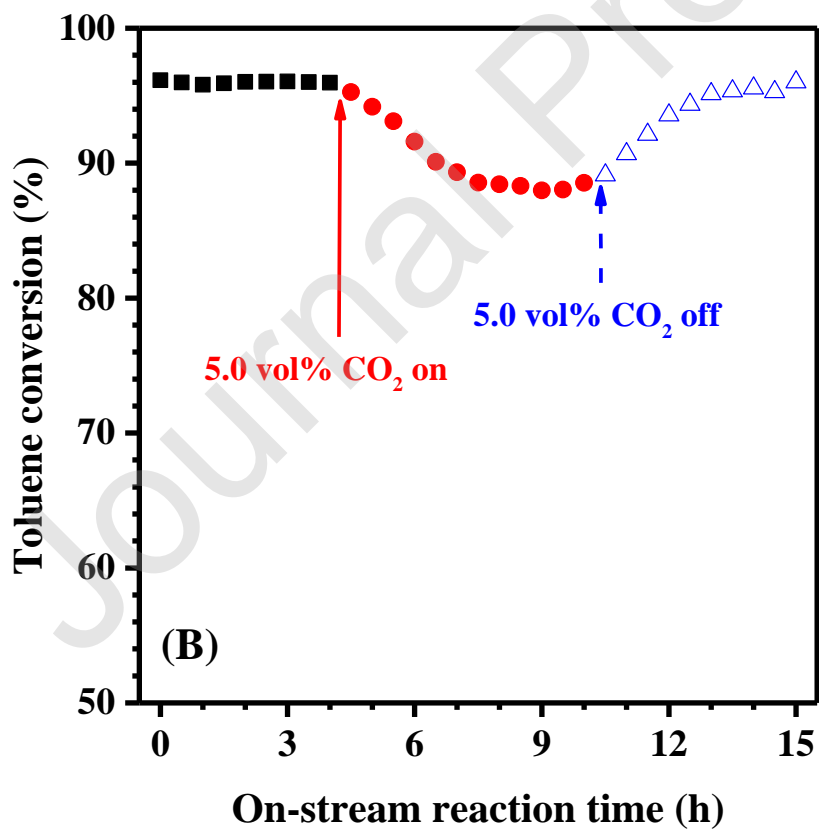
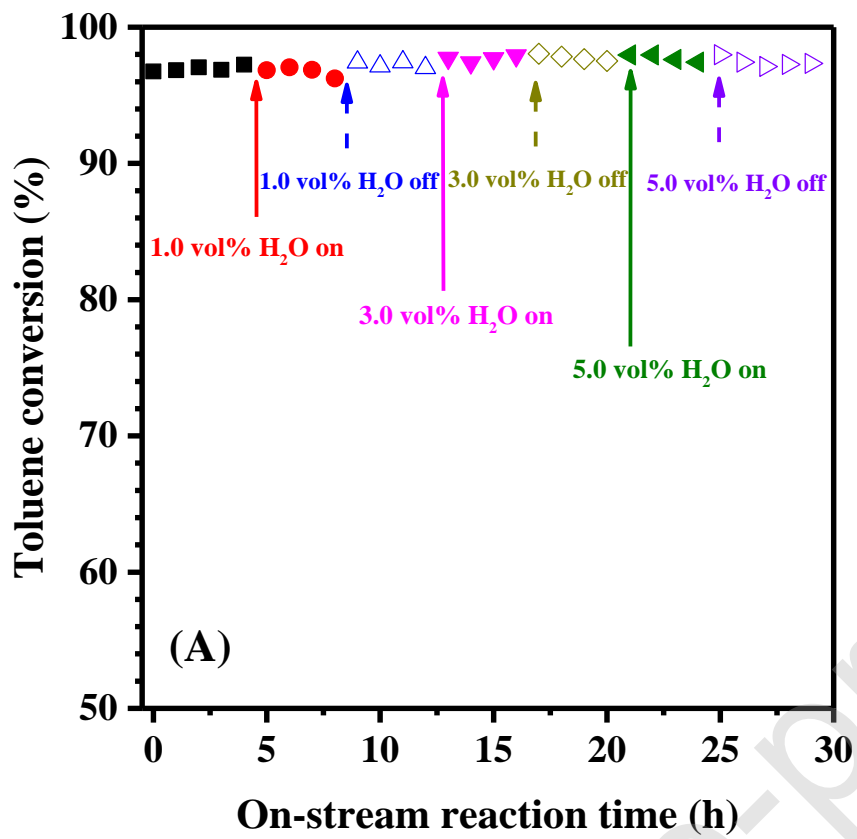


Fig. 8. Effects of (A) H₂O and (B) CO₂ on catalytic activity of 0.37Pt–0.16MnO_x/meso-CeO₂ at 180 °C and SV = 40,000 mL/(g h).

Journal Pre-proof

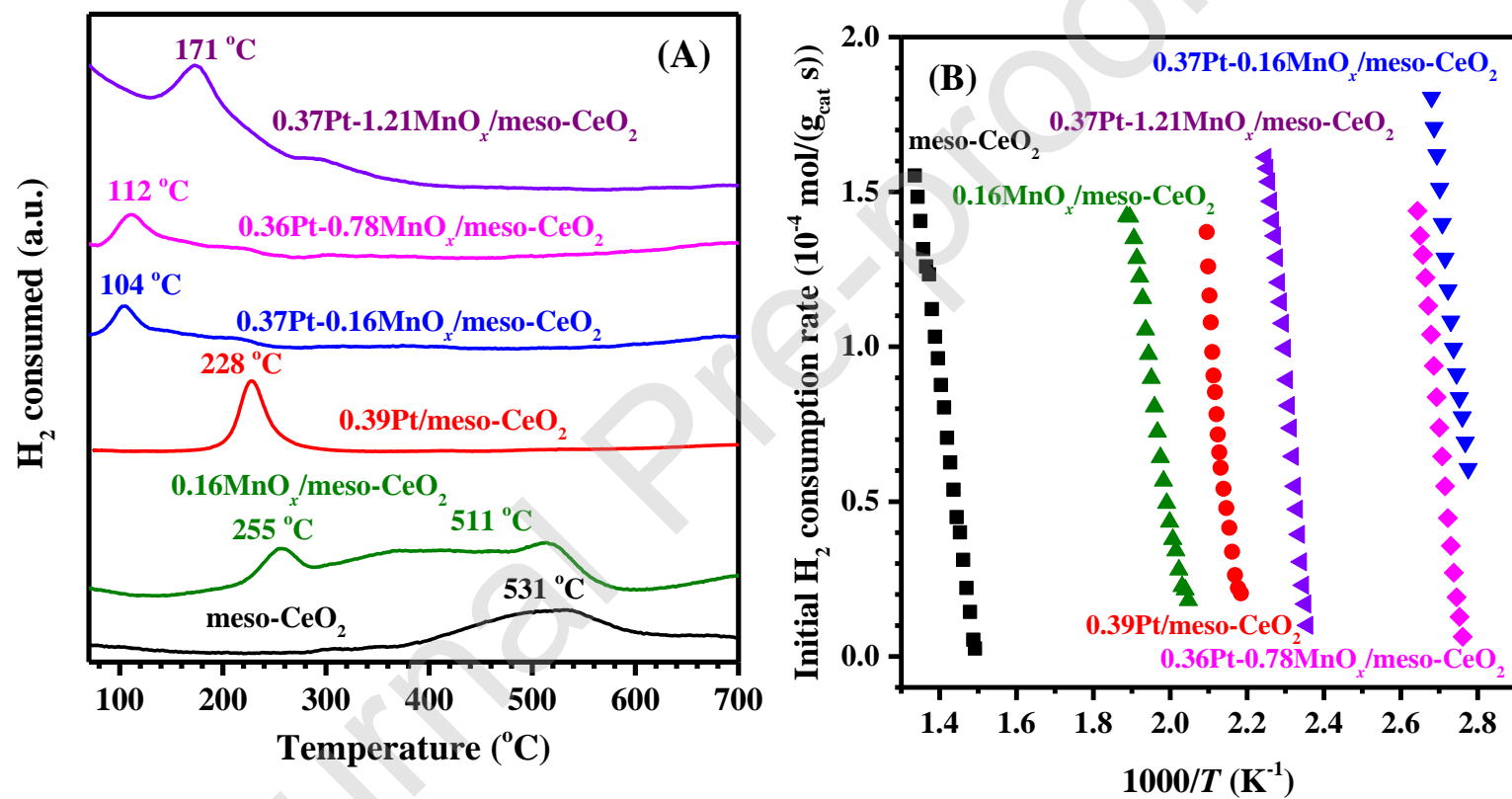


Fig. 9. (A) H₂-TPR profiles and (B) initial H₂ consumption rate as a function of inverse temperature of the samples.

as a function of

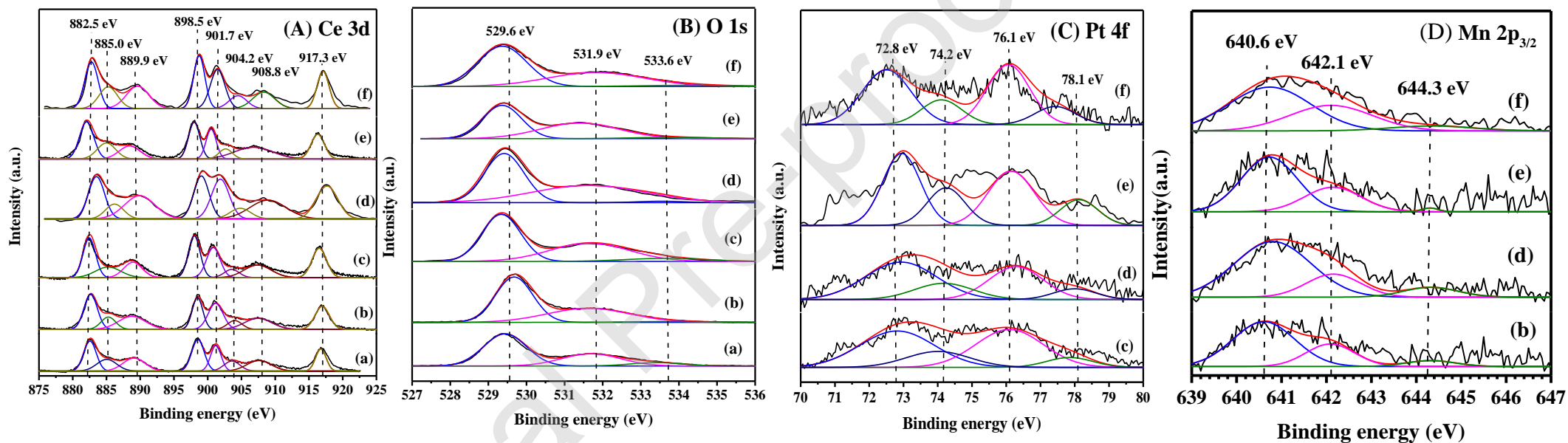


Fig. 10. (A) Ce 3d, (B) O 1s, (C) Pt 4f, and (D) Mn 2p_{3/2} XPS spectra of (a) meso-CeO₂, (b) 0.16MnO_x/meso-CeO₂, (c) 0.39Pt/meso-CeO₂, (d) 0.37Pt–0.16MnO_x/meso-CeO₂, (e) 0.36Pt–0.78MnO_x/meso-CeO₂, and (f) 0.37Pt–1.21MnO_x/meso-CeO₂.

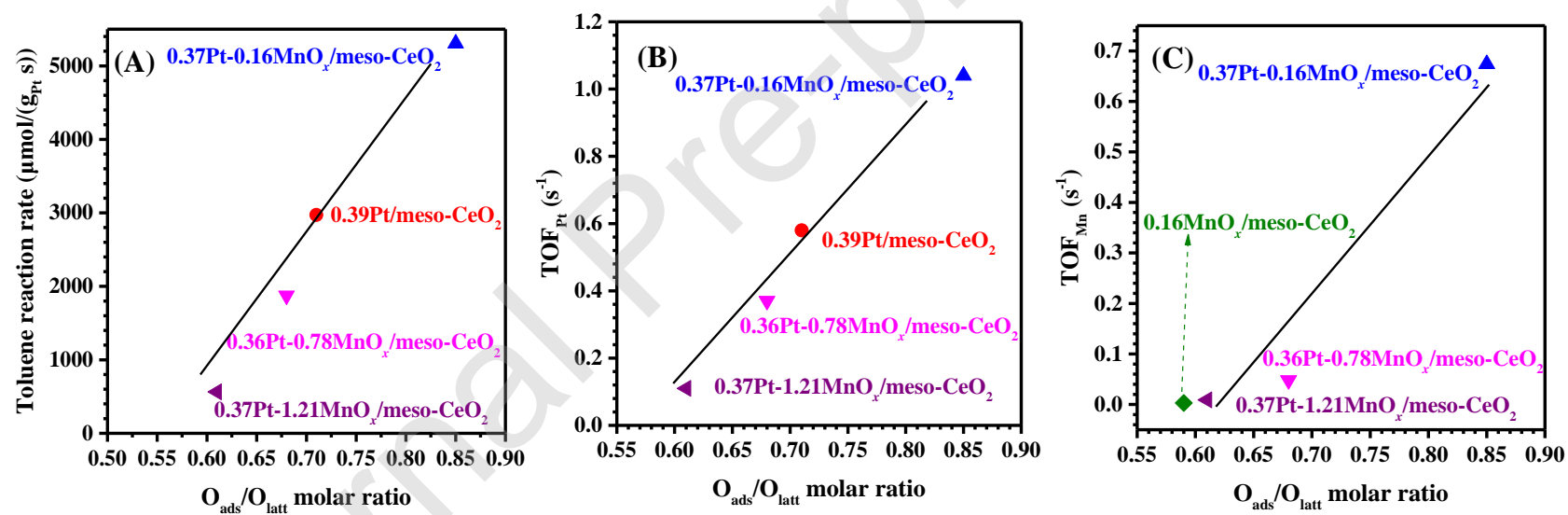


Fig. 11. (A) Toluene reaction rate versus O_{ads}/O_{latt} molar ratio, (B) TOF_{Pt} versus O_{ads}/O_{latt} molar ratio, (C) TOF_{Mn} versus O_{ads}/O_{latt} molar ratio of the samples for toluene combustion at 160 °C and $\text{SV} = 40,000 \text{ mL}/(\text{g h})$.

Journal Pre-proof

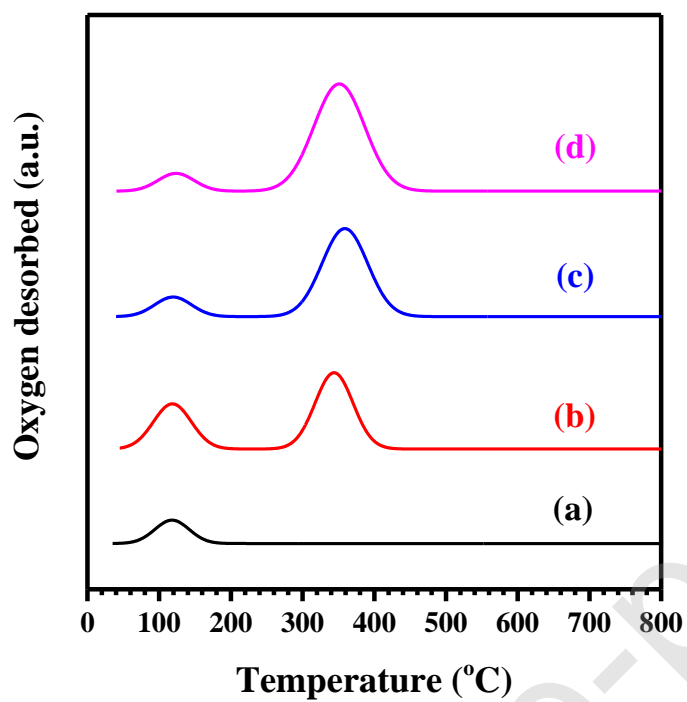


Fig. 12. O₂-TPD profiles of (a) 0.39Pt/meso-CeO₂ (b) 0.37Pt–0.16MnO_x/meso-CeO₂, (c) 0.36Pt–0.78MnO_x/meso-CeO₂, and (d) 0.37Pt–1.21MnO_x/meso-CeO₂.

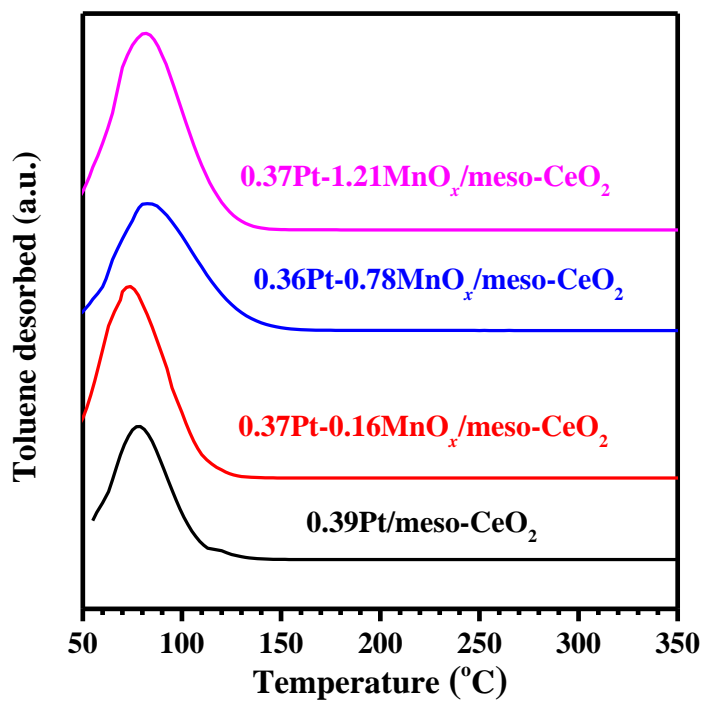
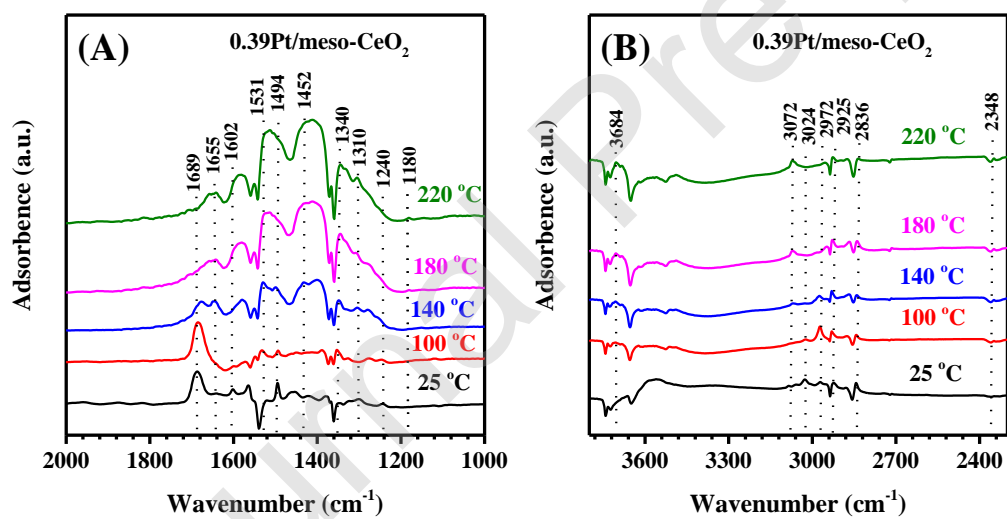


Fig. 13. Toluene-TPD profiles of the samples.



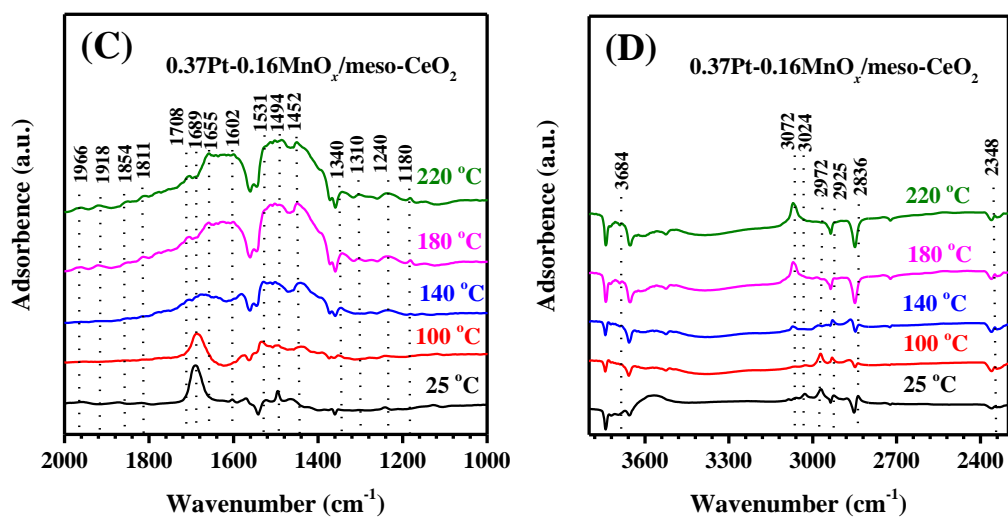


Fig. 14. In situ DRIFTS spectra of (A, B) $0.39\text{Pt}/\text{meso-CeO}_2$ and (C, D) $0.37\text{Pt}-0.16\text{MnO}_x/\text{meso-CeO}_2$ during toluene combustion at different temperatures (reaction conditions: 1000 ppm toluene + 20 vol% O_2 + N_2 (balance); $\text{SV} = 40,000 \text{ mL}/(\text{g h})$).